Molybdenum Disulfide Nanodisks for Photoelectrochemical Hydrogen Evolution

Presented to
The Academic Faculty

by

Marshall Clark Tekell

In Partial Fulfillment
of the Requirements for the Bachelor of Science in
Chemical Engineering in the
Cockrell School of Engineering

The University of Texas at Austin
May 2019

Molybdenum Disulfide Nanodisks for Photoelectrochemical Hydrogen Evolution

Approved by:

Dr. Donglei (Emma) Fan, Advisor
Department of Mechanical Engineering
The University of Texas at Austin

Dr. Yuanyue Liu
Department of Mechanical Engineering
The University of Texas at Austin

Date Approved: April 29, 2019

ACKNOWLEDGEMENTS

Thank you to Professor Donglei Fan, Yun Huang, Weigu Li, Jianhe Guo, and all of the researchers in the Nanomaterial Innovation Lab. Thank you to the Friends of Alec and T.W. Whaley for your generous contribution to my education and the education of others. Thank you to the Waco Independent School District Education Foundation and Valda McWhirter for your investments in my education and the education of others. Thank you Professor Yuanyue Liu for agreeing to serve as my second reader. Thank you to Gabriel Cosssio and Professor Edward Yu for your help with the polystyrene nanospheres. Thank you to Anna Dorfi at Columbia University for your suggestion to use Electroplater's Tape.

TABLE OF CONTENTS

ABSTRACT

Current strategies of energy production and conversion continue to emit CO_2 at a rate that is extremely likely to warm the planet 1.5°C by 2052, and energy sourced from renewables needs to increase 95% by 2050 in the most relaxed reductions emissions scenarios. Photoelectrochemical (PEC) hydrogen evolution from MoS_2/p-Si is introduced as a technology that can directly convert solar energy to chemical energy without the use of rare earth metals. The mechanisms of both hydrogen evolution from 2H-MoS_2 edge sites and semiconductor photocatalysis are discussed. Colloidal lithography using masks of polystyrene (PS) nanospheres, electron-beam deposition, and chemical vapor deposition were used to control the diameter (200–500 nm), thickness (1.5–9.5 nm) and areal density (1.8–20.9%) of MoS_2 nanodisks on p-Si, which were characterized using scanning electron microscopy (SEM), atomic force microscopy (AFM), Raman spectroscopy, and image processing techniques. The PEC performances of bare p-Si and MoS_2/p-Si were analyzed using linear scan voltammetry (LSV) and chronoamperometry (CA). Replacing Ga-In with Au as the back contact for p-Si in PEC testing was found to reduce the magnitude of the overpotential at -10 mA cm^{-2} from -593 to -390 mV due to Schottky barrier removal. 200 nm MoS_2 and 500 nm MoS_2 nanodisks on p-Si further decreased the overpotential at 10 mA cm^{-2} from -390 mV to -234 and -172 mV, respectively, and produced short-circuit currents of -0.45 mA cm^{-2} and -0.80 mA cm^{-2}, respectively. The stability of MoS_2/p-Si photocathode performance was found to depend on the thickness of e-beam deposited Mo, with a 31 and 134 mV decrease in overpotential measured for 500 nm MoS_2 nanodisks produced from 1 nm and 4 nm Mo, respectively. Finally, the *in situ* observation of hydrogen evolution from bare p-Si was demonstrated, and images were collected of bubbles on the microscale. Future work involves optimizing the thickness of MoS_2 to meet state-of-the-art performance parameters and investigating the conditions under which the growth of insulating SiO_2 affects photocathode performance.

CHAPTER 1. Introduction

1.1 Motivation

The International Energy Agency (IEA) estimates that the global Total Final Consumption (TFC) of energy in 2016 was 4 x 10^{20} J, which corresponds to an average rate of 12.7 TW.[1] The majority (66.8%) of energy consumption comes from oil (40.9%), natural gas (15.1%), and coal (10.8%).[1] In 2016, these three sources were responsible for 99.3% percent of the 32 billion metric tons of carbon dioxide (CO_2) that were released into the atmosphere, which corresponds to an average rate of 1.0 million kilograms per second.[1] Due to industrialization in developing countries, global energy consumption is expected to increase 28% by 2040, and emissions of CO_2 are expected to rise 22% by 2040.[2] In 2014, the United Nations' Intergovernmental Panel on Climate Change (IPCC) concluded that it was extremely likely that the anthropogenic release of CO_2 was responsible for more than half of the measured increases in global average surface temperature from 1951 to 2010.[3] The cumulative emissions of CO_2 from the beginning of the industrial era to the near present have already increased global mean surface temperature by approximately 1.0°C relative to the average temperature in the second half of the 19th century.[4] Projections of current trends suggest that 1.5°C of anthropogenically induced global warming is statistically very likely between 2030 and 2052.[4] **Figure 1** shows the clear relationship between cumulative CO_2 emissions and increase in global mean surface temperature. The colored portions of the graph represent the predictions of a range of climate models under different emissions reduction strategies. The black data shows the measured warming that has already occurred. Thus, there is a clear link

between CO_2 emissions from current strategies of energy consumption and significant increases in global mean surface temperature.

The impact from the cumulative CO_2 emissions from the industrial era to the present day will persist for millennia, even in the most aggressive emissions reduction scenarios, due the variable timescales of response for different environmental systems and phenomena.[3] Sea levels, for example, are expected to rise between 0.26 and 0.77 m by 2100 at 1.5°C of anthropogenic global warming, and levels will continue to rise for hundreds or thousands of years after 2100.[4] But, other effects will be more immediate; negative effects of 1.5°C include declining crop and fishery yields, increased frequency and magnitude of populations displaced by extreme weather events, the irreversible loss of coral reefs and Arctic ecosystems, amplified impacts of urban heat waves, increased spread of vector-borne diseases, and increased populations of people susceptible to poverty.[4] Dramatic and immediate emissions reduction strategies are necessary to keep global warming below 4.0°C by 2100,[3] and, even in the most relaxed emissions scenarios, the median percentage of energy generated by low-carbon technologies will need to increase 95% before 2050.[4] Furthermore, society has an ethical responsibility to preserve the natural environment for future generations hundreds or thousands of years into the future, and continuing to deplete supplies of fossil fuels and emit vast amounts of CO_2 in the atmosphere is clearly unsustainable for both the planet in the near future and for the human enterprise in the distant future. Current trends in energy consumption, therefore, will have dramatic impacts on the key environmental factors that facilitate continued economic development and improvements in the global quality of life. Replacing fossil fuels with carbon-neutral, renewable forms of energy while still maintaining the current clip of energy consumption is the foremost challenge posed to mankind in the 21st century and beyond.

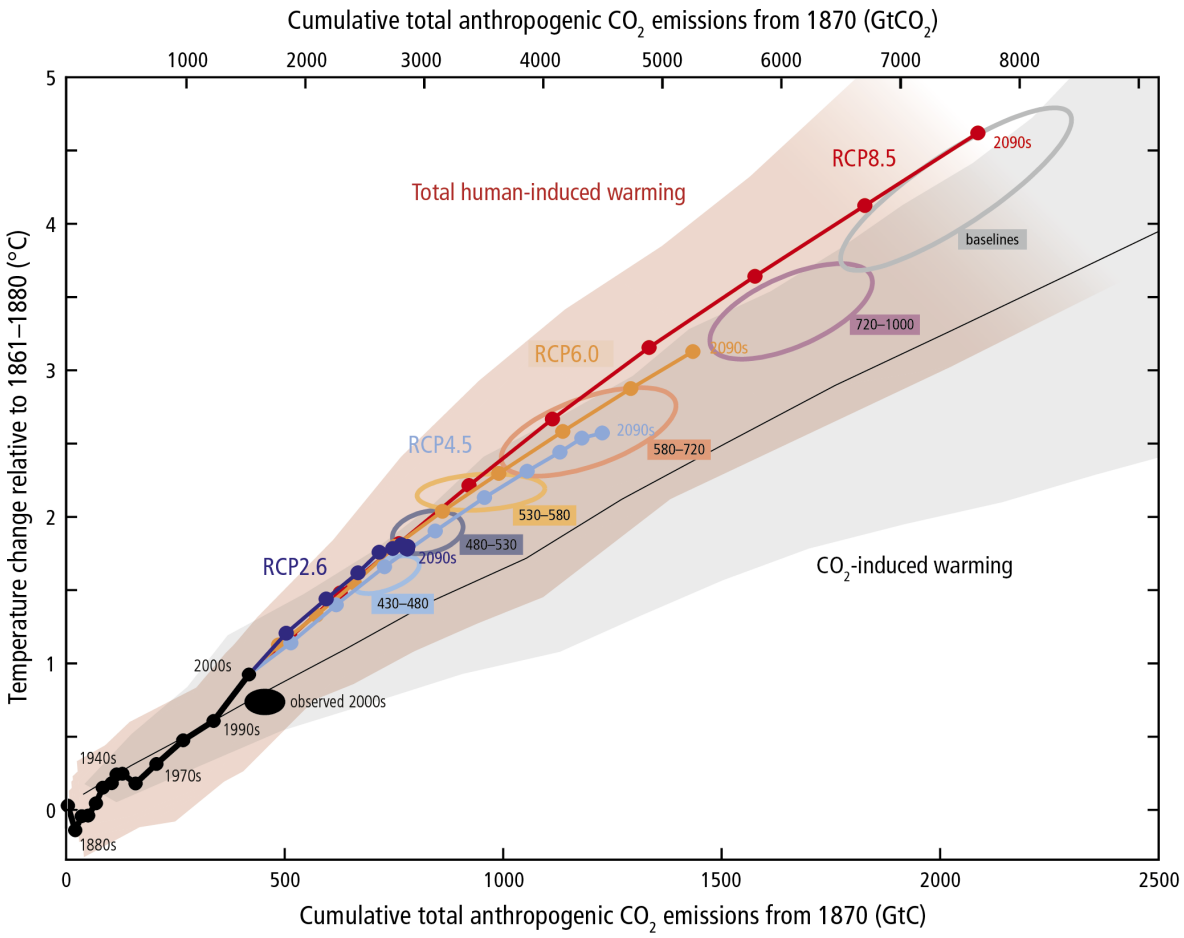

Figure 1: Reproduced from the IPCC Climate Change 2014 Synthesis Report.[3] Colored sections represent the range of current climate models. Ellipses represent ranges of CO_2 PPM at cumulative emissions. Temperature refers to global mean surface temperature. Representative Concentration Pathways (RCPs) represent different emissions mitigation scenarios. Black filled circles represent measured data to date.

The current platform for renewable sources of energy includes a suite of technologies—biofuels, hydroelectricity, solar photovoltaics, wind turbines, geothermal, and others—that convert ambient and virtually inexhaustible forms of energy into grid electricity for expedient human consumption. Of these technologies, biofuels remain the most significant in terms of overall energy consumption; in 2017, biofuels provided four times the energy of solar photovoltaics and wind turbines combined.[5] Still, solar photovoltaics continue to expand to

generate a larger share of the world's electricity. Halfway through 2016, about 1% of the electricity in the United States came from solar photovoltaics, up from less than 0.1% in 2011.[6] Solar photovoltaic capacity continues to expand at a faster pace than all other renewable energy technologies combined, with most of the world's installed capacity in China, Japan, the United States, and Europe.[5] Recently, gains in installed solar energy capacity have benefited immensely from distributed generation; placing photovoltaics near the end users of power reduces losses from electricity transmission and allows integrated energy storage systems to mitigate the technology's inherent intermittency.[5, 6] In 2017, the United States Department of Energy identified low-cost solar energy storage as a necessary tool to expand solar power implementation in the coming decades.[6] Indeed, intense research efforts have been devoted to increasing the energy density, power density, large-scale manufacturability, and affordability of electrochemical energy storage technologies like Li-ion batteries and supercapacitors to increase the feasibility of solar photovoltaics both at the point of generation and at the point of end-use.

Despite advancements in electrochemical energy storage technologies, there exists demand for energy-dense liquid fuels for use in transportation systems—long-distance land travel, air travel, and aerospace travel—and off-grid applications. The gravimetric and volumetric energy densities of the most advanced Li-ion batteries are still two orders of magnitude below those of gasoline and diesel.[7] In order to supplant the use of fossil fuels, chemical engineers need to develop fuels that can be integrated with existing, intermittent sources of renewable electricity and that can be stored safely and cost effectively at high densities for on-demand and off-grid applications. Scientists and engineers have developed electrochemical and photoelectrochemical energy conversion technologies to fill this gap and

to create fuels from solar energy. Electrocatalytic surfaces that can convert dissolved CO_2 in aqueous solution into value-added hydrocarbons like methanol and formic acid have been demonstrated in the past decade on the lab scale.[8] Other, more developed technologies include catalysts for the hydrogen evolution reaction (HER) and the oxygen evolution reaction (OER) that use electricity to "split" water and generate hydrogen for fuel cells or for industrial chemical processes. Both of these technologies can be integrated with existing solar photovoltaics to complete an indirect solar-to-fuel conversion process. Photoelectrochemistry, however, involves direct conversion of the energy in sunlight to energy stored in chemical bonds by combining a photoabsorber with a catalytic surface and a semiconductor-liquid junction.[9] Converting solar energy to the energy stored in the 1sσ bond in H_2 represents integrated energy generation and storage. Combustion of H_2 in a fuel cell releases this energy and produces water, instead of CO_2, as the only product; therefore, photoelectrochemical hydrogen production represents one step in a energy storage and generation system that begins with water as a feedstock and ends with water as a reaction product.

1.2 MoS_2 for the hydrogen evolution reaction

The hydrogen evolution reaction (HER) combines protons in aqueous solution with electrons supplied via an electrical connection (electrochemical) or via photoexcitation of a semiconductor (photoelectrochemical) to produce hydrogen gas, H_2. The reaction can proceed through one of two mechanisms, which both have the same first step:

(1) $H^+_{(aq)} + e^- + * \leftrightarrow H^*$ (Volmer)

(2) $2H^* \leftrightarrow H_{2\,(g)}$ (Tafel)

(3) $H^* + e^- + H^+ \leftrightarrow H_{2\,(g)}$ (Heyrovsky)

where H^+ represents an aqueous proton, $*$ represents an active site for adsorption, e^- represents the electron supplied via electrical connection or via photoexcitation, and H^* represents a proton adsorbed onto an active site. Detailed studies of the mechanism of hydrogen evolution at metal surfaces in contact with electrolytes of varying pH have been conducted since the 1950s,[10, 11] but the exact contributions of each mechanistic pathway to the observed current is still the subject of active research in the field.[12] In the design of electrocatalysts, however, it is only necessary to optimize the shared Volmer step, which describes the strength with which the catalytic material adsorbs protons from solution. First suggested by Parsons in 1958, the change in Gibbs free energy, ΔG_H, of the hydrogen adsorption step determines the exchange current density.[10] The material should not adsorb protons too weakly to prevent desorption before reaction or too strongly to prevent high occupation of adsorption sites and catalyst poisoning.[13] Therefore, pioneering works in the early 2000s used density functional theory (DFT) to conduct high-throughput computational screening of potential HER materials to identify materials with $\Delta G_H \approx 0$.[13, 14] The resulting Sabatier or volcano plot, shown in **Figure 2**E, indicates that $\Delta G_H \approx 0$ maximizes the magnitude of the logarithm of the exchange current density.[14]

These studies identified platinum (Pt) as the highest-performing catalyst for the hydrogen evolution reaction. The standard reduction potential of hydrogen on a Pt surface is defined as the reference point for most electrochemical systems because the kinetics and thermodynamics are reliable and well understood. But, because of Pt's scarcity and high cost, cheaper materials with similar performance characteristics have been explored both computationally and experimentally to lower the cost of H_2 for grid-scale applications. As shown in **Figure 2**E, density functional theory (DFT) simulations conducted by Jaramillo, *et*

al. identified molybdenum disulfide (MoS_2), a two-dimensional (2D) transition metal dichalcogenide (TMD), as potential replacement for Pt in HER. TMDs are composed of a transition metal (Mo, W, Co, Ni, etc.) and a chalcogenide (S, Se, or Te) and have the formula MX_2. MoS_2 has two relevant polymorphs: metallic 1T-MoS_2 and semiconducting 2H-MoS_2, shown below in **Figure 2**A. Importantly, in 2H-MoS_2 the atoms arrange in 2D layers that stack together via van der Waals forces to form bulk crystals with an interlayer spacing of 0.65 nm, as shown in **Figure 2**C. The landmark study by Jaramillo *et al.* reported a linear correlation between the areal density of Mo-edge sites that terminated 2H-MoS_2 monolayers and electrocatalytic activity for HER.[14] Therefore, in the past decade, significant research effort has been devoted to optimize the performance of the MoS_2 and other TMDs via morphologies that preferentially expose catalytically active sites,[15-19] doping of other transition metals,[20] and post-synthetic defect engineering.[21-23] Shown in **Figure 2**D, the substitutional doping of Co for a Mo or W can theoretically activate the S-edge sites for HER. The ΔG_H at the Mo- or W-edge sites remain unaffected, but the ΔG_H for the S-edges are reduced from 0.18 to 0.10 eV and from 0.22 eV to 0.07 eV for Co-doped MoS_2 and WS_2, respectively.[20] **Figure 2**B is a schematic of HER occurring at the terminating edge sites of monolayer MoS_2. Shi *et al.* used low-pressure chemical vapor deposition (LPCVD) to control the growth of microscale triangular monolayers at different coverages and, again, showed a linear correlation between areal density of edge length and exchange current density. Other studies have activated the 2H basal plane of MoS_2 for HER using post-synthetic oxygen plasma exposure[21] and strained sulfur vacancies.[22]

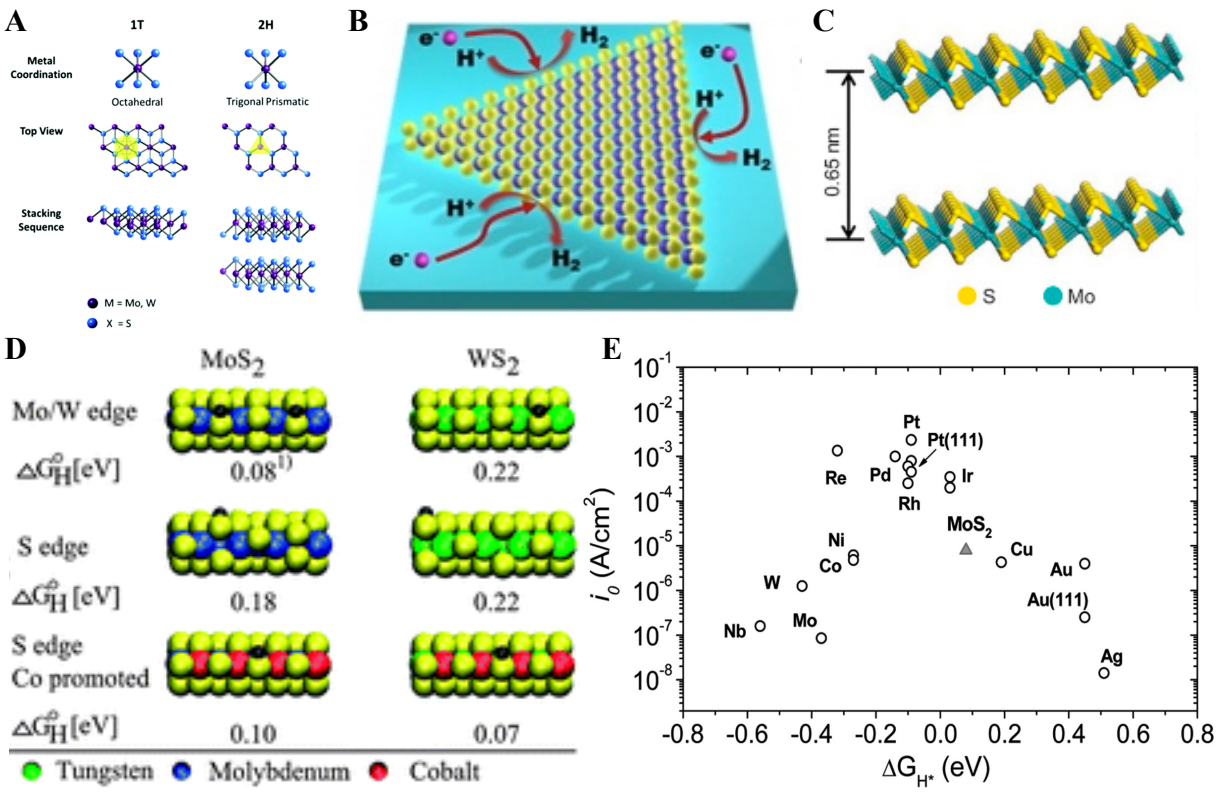

Figure 2: A: Metal coordinations and stacking sequences of TMD unit cells. The metallic 1T phase has octahedral coordination and AbC stacking. The 2H phase has trigonal prismatic coordination and AbA BaB (2H) stacking.[24] **B:** Triangular monolayers of MoS_2 grown via LPCVD expose active Mo-edge sites to protons in electrolyte for HER.[25] **C:** van der Waals stacking of 2H-MoS_2 monolayers lead to the formation of a bulk crystal. The interlayer stacking distance is estimated to be ~0.65 nm.[26] **D:** DFT calculations reveal that Co-doping can reduce the ΔG_H of the Volmer step for the S-edge in 2H TMDs.[20] **E:** DFT calculations reveal that Pt is the ideal material for the HER, as shown in this Sabatier plot reproduced from Jaramillo *et al.*[14] MoS_2, gray triangle, has been identified as a possible replacement for Pt in grid-scale applications.

The two main figures of merit for comparing electrocatalysts for HER are the Tafel slope and overpotential required to meet a defined current density. The Butler-Volmer equation describes the kinetics of electrochemical reactions:

$$(4)\ i = i_0\left(\exp\left[\frac{\alpha_a nF\eta}{RT}\right] - \exp\left[\frac{\alpha_c nF\eta}{RT}\right]\right)$$

where i is the current density (mA cm^{-2}), i_0 is the exchange current density (mA cm^{-2}), α is a transfer coefficient, n is the number of electrons transferred per reaction, F is Faraday's constant, η is the overpotential (V), R is the gas constant, and T is the temperature.[27] The exchange current density, mentioned earlier in the context of computational screening, determines the intrinsic rate of electron transfer between the electrocatalytic surface and the electrolyte. The overpotential η refers to the electrode potential used to drive the reaction and is the abscissa in linear scan voltammograms (LSVs). It is usually reported relative to the reference potential of HER at Pt, which is defined as 0.0V. The two exponentials in (4) represent the anodic and cathodic reactions and the constants associated with each can be lumped together in the following form:

(5) $i_a = i_0 \exp\left(\frac{\eta}{b}\right)$

(6) $i_c = -i_0 \exp\left(-\frac{\eta}{b}\right)$

where the subscripts a and c denote the anodic and cathodic reactions, respectively, and b is the Tafel slope. At overpotentials far from equilibrium, the cathodic or anodic term dominates and experimental data can be fitted to determine the Tafel slope and the exchange current density.[27] Developing cheap, stable electrocatalysts with low Tafel slopes and high exchange current densities is the subject of active research, and the figures of merit are often compared to those of Pt, which is considered the ideal material.[28]

1.3 Photoelectrochemical hydrogen evolution

1.3.1 Device design for photoelectrochemical water splitting

Photoelectrochemical (PEC) systems follow the same principles as electrochemical systems but incorporate semiconducting photoabsorbers. PEC water splitting consists of two reactions, HER at the photocathode and OER at the photoanode. Most experimental PEC devices, however, only use the photoabsorption of a semiconductor to drive one half reaction—either HER or OER—and use a noble metal to complete the circuit within the same electrolyte solution or within a different electrolyte solution separated by an H^+-permeable membrane. This is shown schematically in **Figure 3**A for HER at a photocathode and OER at a metal anode.[29] Practical implementation of PEC water splitting, however, requires a device construction similar to that shown in in **Figure 3**B, where one light source drives electrochemical reactions at both the anode and cathode.[30] This device design, proposed by Warren *et al.* utilizes high-energy, blue light to drive the photoanode and low-energy, red light to drive the photocathode. Recently, Davis *et al.* proposed a indirect, photovoltaic-driven water splitting system to collect O_2 and H_2 in separate chambers without the use of membranes, as shown in **Figure 3**C.[31] This theoretical discussion and the following discussion of experimental results, however, will focus mainly on the experimental investigation of photocathodic hydrogen evolution with MoS_2 as a catalyst instead of the construction of devices for large-scale generation and collection of H_2 for fuel.

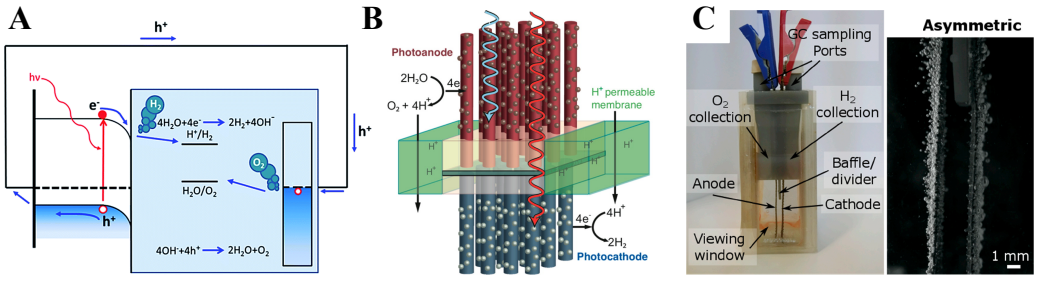

Figure 3: A: Experimental set-up for photocathode. Irradiation and photogenerated electron-hole pair is shown in red. Electrons are driven to the SCLJ to participate in HER, while holes

are driven to the metal anode to participate in OER (right).[29] **B:** PEC device proposed by Warren *et al.* High-energy visible irradiation (blue) drives the photoanode, while low-energy visible irradiation (red) drives the photocathode.[30] **C:** Membraneless PV-driven electrolyzer for water separation. Device construction (left) allows for the asymmetric collection of O_2 and H_2.[31]

1.3.2 Basic physical principles of semiconductor photoelectrochemistry

The working principles of the photocathode and photoanode in PEC systems both depend on band bending at the semiconductor-electrolyte junction (SCLJ). The redox potential of the electrolyte and the Fermi level of the semiconductor equalize upon contact with the spontaneous transfer of electrons.[32, 33] At the photocathode, a p-type semiconductor, electrons transfer to the valence band from the redox pair in the electrolyte, creating a downward-bending depletion region near the surface, *i.e.* a spatial distribution of negative charges (**Figure 4**D). The opposite is true at the photoanode, an n-type semiconductor; electrons in the conduction band enter states in the electrolyte and create an upward-bending depletion region (**Figure 4**E). In both cases, the band gap remains the same, so both the conduction and valence bands bend downward (p-type) or upward (n-type) in energy. The formation of depletion layers can be described with Poisson's equation (7) and the abrupt depletion approximation, which assumes a step-change in the density of charges near the SCLJ equal to the dopant density in the semiconductor, N_D (**Figure 4**A). Integrating Poisson's equation across the depletion region, then, produces (8) where W_{SC} is the width of the space-charge region, q is the elementary charge, and ε_s is the static dielectric constant of the semiconductor.[33, 34] The negative first-derivative of the potential equals the electric field in the space charge region, which, as shown in (8), varies linearly with x, the distance from the SCLJ (**Figure 4**B).

$$(7)\ \frac{\delta^2\varphi}{\delta x^2} = -\frac{\rho}{\varepsilon_s} = -\frac{qN_D}{\varepsilon_s}$$

(8) $-\frac{\delta\varphi}{\delta x} = \frac{qN_D}{\varepsilon_s}x = E$ for $0 \leq x \leq W_{SC}$

Integrating (8) again reveals the parabolic potential profile in the space-charge region and an expression for the width, W_{SC}, as a function of the dopant density and the change in potential across the space-charge region $\Delta\varphi_{SC}$ (9) (**Figure 4**C). The built-in potential is equal to the difference between the Fermi level potential of the semiconductor, E_F, and the redox potential of the electrolyte, E_{H^+/H_2}, which can altered during a PEC test in a three-electrode set-up (10).

(9) $W_{SC} = (\frac{2qN_D\Delta\varphi_{SC}}{\varepsilon_s})^{1/2}$

(10) $\Delta\varphi_{SC} = \frac{|E_F - E_{H^+/H_2}|}{q}$

The energy gap between the valence and conduction bands remains constant, and the parabolic potential profile is present in both bands near the SCLJ. As a result of the potential profile, the band profiles bend as they approach the SCLJ, as shown in **Figure 4**D for p-Si, where $\Delta\varphi_{SC} = \psi_S$. W_{SC} varies between 20 and 10,000 Å depending on the doping level of the semiconductor.[35] Electron tunneling through the space-charge region, therefore, is only possible in highly doped semiconductors. The charging of the space-charge layer is analogous to the charging of a capacitor, as a layer of opposite charge in the electrolyte screens the semiconductor surface.[33] The distribution of charge from the SCLJ into the electrolyte can be divided into three different planes, shown in **Figure 4**F.[36] The inner Helmholtz plane (IHP) passes through the center of adsorbed ions, the outer Helmholtz plane (OHP) passes through the center of solvated ions, and the diffuse or Guoy-Chapman layer represents the remaining the potential drop between the OHP and the bulk electrolyte.[37]

The Fermi level of doped n-type and p-type semiconductors can be calculated from (11) and (12), respectively, where n and p are the dopant concentrations, E_c represents the conduction band energy, E_V represents the valence band energy, N_c is the density of states in the conduction band, and N_V is the density of states in the valence band.[34]

(10) $n = N_C \exp\left(-\frac{E_c - E_F}{k_b T}\right)$

(11) $p = N_V \exp\left(-\frac{E_V - E_F}{k_b T}\right)$

When the semiconductor absorbs light with an energy greater than that of its band gap, $E_g = E_c - E_v$, an electron-hole pair is generated and the minority carrier is available to participate in an electrochemical reaction. Lambert-Beer's law, shown in (12)[37] dictates the optical absorption in semiconductor materials, with an absorption coefficient, α, specific to the material and proportional to energy of the irradiation (14-15).[38]

(12) $I(x) = I_0 \exp(-\alpha x)$

(13) $\alpha \propto (E_{ph} - E_g)^{1/2}$ (direct band transition)

(14) $\alpha \propto (E_{ph} - E_g)^2$ (indirect band transition)

The quantity of photogenerated electron-hole pairs is equal in the valence and conduction band, $\Delta n = \Delta p$, and their lifetime, τ_{min}, depends on the initial dopant density and the density of trap states in the band gap. Importantly, the minority recombination length, L_{min}, given by (15) must be longer than the absorption depth of the semiconductor in order for the minority carrier to participate in electrochemical reactions at the SCLJ.[34, 37]

(15) $L_{min} = (D_{min}\tau_{min})^{1/2}$

D_{min} represents the minority carrier diffusion coefficient, which increases with the purity of the semiconductor. This imposes additional material requirements for PEC; cheaper, polycrystalline cells cannot be used because of their small minority carrier recombination lengths.[39]

The thermodynamics of the electrochemical reactions at the SCLJ depend on the different between the quasi-Fermi level of the minority carrier and the redox potential of the electrolyte. When electron-hole pairs are created in a quantity, $\Delta n = \Delta p$, the Fermi level of the minority carrier changes significantly. For a p-type semiconductor, $\Delta p \ll p$, the quasi-Fermi for the photogenerated hole, $E_{F,p}$ does not differ signficantly from that of the dark material, E_F. The concentration of minority carriers, however, increases by several factors of magnitude, $\Delta n \gg n$. The resulting quasi-Fermi level, $E_{F,n}$, given by (16-17), falls in the band gap, as shown in bottom left of **Figure 5**B.[30, 37]

$$(16) \quad n + \Delta n = N_C \exp\left(-\frac{E_c - E_{F,n}}{k_b T}\right)$$

The difference between the chemical potential, *i.e.* quasi-Fermi level, of the photogenerated minority carrier and that of the majority carrier, which is equal to the redox pair in the electrolyte, provides the thermodynamic driving force for the electrochemical reduction reaction at the SCLJ and determines the maximum performance of photocathodes. The engineer's job, then, is to design a system that extracts the greatest portion of this difference in chemical energy.[40]

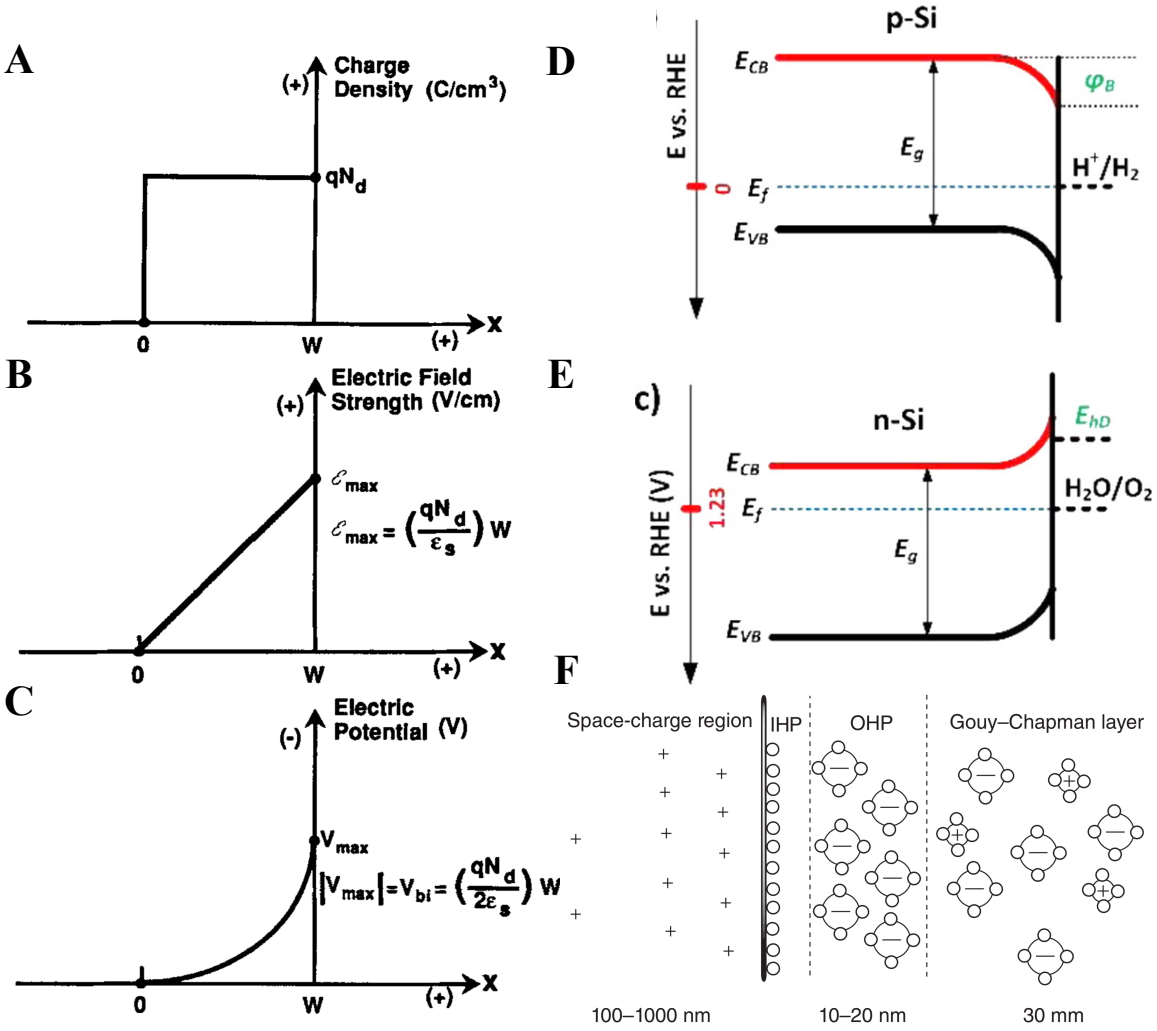

Figure 4: A: Abrupt depletion approximation which sets the charge density in Poisson's equation equal to qN_D, product of the charge of carriers in the space-charge region and the dopant density. **B:** Integrating Poisson's equation produces an expression for the electric field, which reaches its maximum at the SCLJ. **C:** A second integration reveals the potential profile, which describes the built-in voltage and band bending. **D:** Chemical potential of electron (Fermi) equilibration between the semiconductor and the redox pair creates downward bending bands in p-Si due to a negative space-charge region. **E:** The opposite is true for n-Si, shown here at a bias potential equal to the redox potential for OER. **F:** Illustration of charge distribution for band-bending case shown in E. The space-charge region is screened by ions in the inner Helmholtz plane (IHP), outer Helmholtz plane (OHP), and diffuse Guoy-Chapman layer. A-C reproduced from Tan *et al.*[33] D-E reproduced from Sun *et al.*[41] F reproduced from Kisch.[36]

Photogenerated minority carriers, however, must be driven to the SCLJ for this chemical potential energy to be extracted. The measured photocurrent for the photocathode,

therefore, depends on the gradient of the potential due to band bending, the gradient of the minority carrier chemical potential, and the rate of recombination at surface states. The overall photogenerated current can be expressed as a linear combination of contributions from the gradient in chemical potential and the gradient in electrical potential.[34, 42] Due to band bending at the SCLJ and under the abrupt depletion approximation, we can assume a linear electric field in the space-charge region (8). For a minority electron in the conduction band, this electric field produces a "drift" current proportional to the conductivity, σ (17). The gradient of the electrochemical potential, *i.e.* the change with x of the quasi-Fermi level, $E_{f,n}$, also produces a "diffusion" current proportional to σ. The "drift" and "diffusion" currents can be expressed together (19) to obtain the theoretical photocurrent for a given system.[42]

$$(17)\ j_{drift} = \sigma E = -\sigma \frac{\delta \varphi}{\delta x} = -\sigma \frac{qN_D}{\varepsilon_s} x$$

$$(18)\ j_{diffusion} = -\frac{\sigma}{q}\frac{\delta \mu}{\delta x} \text{ where } \mu_n = E_{f,n} \text{ and } \mu_p = -E_{f,p}$$

$$(19)\ j = j_{drift} + j_{diffusion} = -\frac{\sigma}{q}\left[\frac{q^2 N_D}{\varepsilon_s} x + \frac{\delta E_{f,n}}{\delta x}\right]$$

This result of (19) indicates that photogenerated electrons carriers in regions of the semiconductor near the edge of photoabsorption will be driven by the diffusion current to regions where there is no photoabsorption. For a photocathode at a SCLJ, both the electric field from band bending and the partial photoabsorption given by (12) drive minority electrons to the SCLJ. The theoretical photocurrent, however, is limited by the rate of recombination and, for HER, the kinetic limitations of creating H-H bonds. The effect of surface states and the physics of interfacial electron transfer to open redox states in the solution is worthy of detailed discussion but beyond the scope of this work. For addition information regarding the reader is

referred to textbook[34, 36, 37] discussions on the matter or relevant review articles.[43] However, for the purposes of this work, the discussion of band bending, quasi-Fermi levels, and the resulting current provide insight into physical mechanisms investigated in the following experimental results.

1.3.3 Photooxidation of Si electrodes

Until now, this work has only discussed the fundamentals of PEC water splitting have in terms of the physical effects within the semiconductor. For certain systems, however, the photoabsorption can drive changes in the chemical composition of the photoelectrode. Electrodes for OER are particularly vulnerable to the photooxidation at anodic potentials. n-Si, for instance, has a standard oxidation potential for the formation of insulating SiO_2 well below the standard oxidation potential for OER, as seen below in (20) and (21), where h^+ refer to photogenerated holes in the valence band near the SCLJ.[41]

(20) $Si + 2H_2O + 4h^+ \rightarrow SiO_2 + 4H_{aq}^+ \qquad E \approx -0.85\ V\ vs.\ RHE$

(21) $2H_2O + 2h^+ \rightarrow O_2 + 4H_{aq}^+ \qquad E \approx +1.23\ V\ vs.\ RHE$

At anodic potentials in n-Si, band bending drives photogenerated holes to the surface, where they can react with water to form an insulating oxide that reduces cell performance. Thus, n-Si cannot be used without a protection layer to prevent the growth of an insulating oxide that prevents interfacial electron transfer. Recently, the use of protective layers has also been demonstrated with p-Si photocathodes. Seger *et al.* used a protective layer of TiO_x in order to prevent the growth of SiO_2 at anodic potentials during the electrodeposition of MoS_x as a catalyst for HER (**Figure 5**E).[44] The authors repeatedly cycled bare p/n+ Si and TiO_x-protected

p/n+ Si through a range of oxidative potentials in an electrolyte solution containing the precursors for the electrodeposition. After repeated cycling, only the TiO_x-protected p/n+ Si showed reduction and oxidation peaks consistent with the growth of the MoS_x catalyst (**Figure 5**F). The effect of a protective layer at strictly reductive potentials in p-Si photocathodes, however, has been debated in recent literature. Kwon *et al.* reported cyclic voltammetry measurements of bare p-Si to argue that progressive growth of an oxidation layer reduced the photocurrent with successive cycling and that a full catalyst layer of MoS_2 provided protection from photooxidation.[45] Other groups, too, discuss the reaction of dissolved oxygen in the electrolyte solution to form SiO_2 and suggest that the concentration must be below 15 ppb to prevent the growth of an insulating layer.[46, 47] Chronoamperometry results reported by Choi *et. al.*, however, showed a stable current from bare p-Si at -0.9 V vs. RHE for 6 hr.[48] This conflicts with data reported by Andoshe *et al*. and Kwon *et al.* who both reported the nearly complete loss of photocurrent from bare p-Si well within 6 hr under similar testing conditions.[45, 49, 50] Thus, the value of the protective layer for p-Si photocathodes deserves future research.

1.3.4 Electrode design, buried n^+-p junction, and catalyst heterojunctions

Several design considerations, however, can increase the performance of Si for water splitting. The Lewis group demonstrated that the geometry of the semiconductor electrode could be altered to reduce the required purity of the material. Growing the electrode in microwire geometries reduces the required distance between the photoabsorption event and the SCLJ, reducing the required minority carrier recombination length and allowing the group to use vapor-liquid-solid grown polycrystalline Si instead of monocrystalline wafers.[30, 39] **Figure 5**A (right) shows a cross-section SEM image of the microwire array, with a lightly colored

layer of wax—added to prevent shunts during fabrication—visible closer to the substrate. The image in **Figure 5**A (left) depicts H_2 evolution under solar irradiation and the scale of typical experimental set-ups.[39] The p-Si nanowires can be grown with a radial p-n junction at the SCLJ to increase the thermal energy between the photogenerated electrons and holes. [44] As shown in the bottom right of **Figure 5**B, the photogenerated electrons transfer into the n+ layer at the SCLJ, allowing them to attain chemical potential difference greater than that of the p-Si minority carrier quasi-Fermi level and the dark Fermi level,[34] shown in the bottom left.[30] This increased chemical potential reduces the overpotential required to drive water splitting, which requires a potential difference of about $1.6\,V$ when considering reaction overpotentials and ohmic losses.[41] In addition to improving the thermodynamic driving force for water splitting, the poor reaction kinetics of p-Si for HER require the integration of a catalyst at the SCLJ. In additional to Pt, many groups have explored p-Si/TMD heterojunction photocathodes.[45, 46, 49-52] Shown in **Figure 5**C, Kwon *et al.* created p-Si/2H-MoS_2 as photocathodes for HER.[45] The photogenerated electrons transfer to active sites in MoS_2, where they participate in reactions (1)–(3). The LSVs in **Figure 5**D show the photocurrent responses of the cathodes with varying thickness of the catalyst film, indicating the trade-off between increased reaction kinetics compared to bare p-Si and decreased absorption of light for 29 nm MoS_2. At more cathodic overpotentials, due to mass-transfer limitations of H^+ to the photocathode surface, the photocurrent stabilizes at around -40 mA cm^{-2} for all of the samples tested.

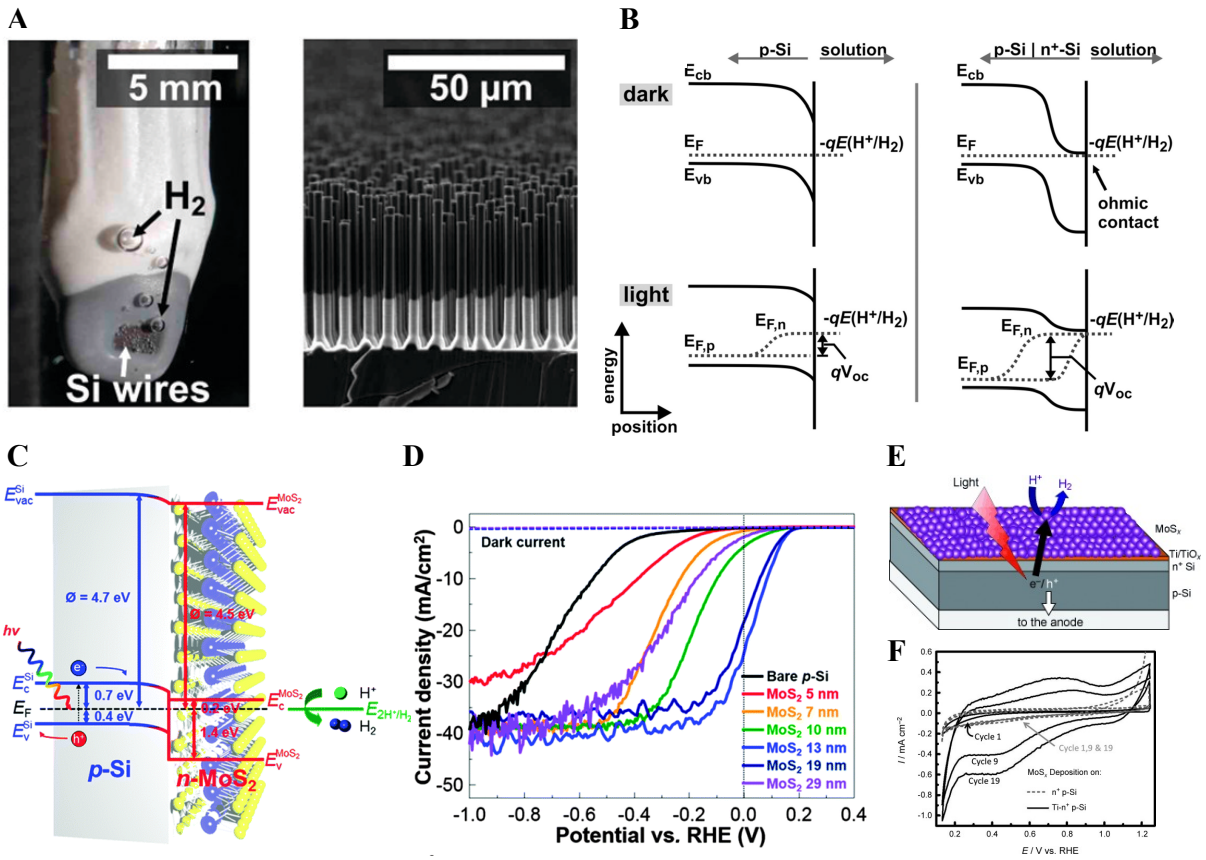

Figure 5: A: (left) H_2 evolution from Pt/Si microwire electrode. Two different types of epoxy are used to isolate photocathodic surface and to prevent the back electrical connection from interacting with the electrolyte. (right) Cross-sectional SEM image of microwire array. Lightly colored wax added to fabrication process to prevent shunting. **B:** Band diagrams demonstrating the effect of p/n$^+$ on photocathode device performance. p/n+ junction decouples p-Si from solution and increases the difference in chemical potential between the electron and hole. **C:** p-Si/MoS_2 heterojunction photocathode. Photogenerated electrons travel to the active sites in 2H-MoS_2 where they reduce hydrogen. **D:** LSVs of p-Si/MoS_2 of different catalyst layer thicknesses. Catalyst layers increase reaction kinetics but decrease photoabsorption. **E:** p-Si/n+-Si/TiO_x/MoS_x stack for protected photocathode. TiO_x prevents growth of SiO_x passivation layer and allows the anodic electrodeposition of MoS_x. **F:** For unprotected p-/n+-Si successive cycling results in the growth of SiO_2 and no MoS_x is electrodeposited (dashed line). For the protected stack (filled line), characteristic oxidation and reduction currents appear for the electrodeposition of MoS_x. **A-B** reproduced from Boettcher *et al.*[39] **C-D** reproduced from Kwon *et al.*[45] **E-F** reproduced from Seger *et al.*[44]

1.4 Summary

Concerns about the consequences of current strategies of energy consumption have incentivized research into renewable energy technologies to meet the aggressive CO_2 emissions mitigations scenarios recommended by the United Nations' Intergovernmental Panel on Climate Change (IPCC). Despite recent growth in the share of grid electricity from photovoltaics, there still exists demand for liquid fuels that can be stored and transported. In this respect, the energy density of the most developed Li-ion batteries lags behind that of fossil fuels. Photoelectrochemical (PEC) water splitting is introduced as a technology that can provide direct storage of solar in chemical bonds to meet the aforementioned challenges. PEC water splitting consists of the hydrogen evolution reaction (HER) at the photocathode and the oxygen evolution reaction (OER) at the photoanode. This work primarily focuses on challenges associated with HER at the photocathode, but discussions of OER at the photoanode are included when theoretical concepts are analogous or when overall device construction is considered. Of the potential catalysts for grid-scale implementation of HER for PEC water splitting, Pt shows the highest performance, both experimentally and theoretically. MoS_2, however, was recently identified as an electrocatalyst that could provide similar performance to Pt at a lower cost and higher abundance. The HER proceeds at the Mo-edge sites that terminate two-dimensional monolayers of MoS_2 and at least two studies have shown linear correlation between the exchange current density and the areal density of Mo-edge sites. Strategies to control the morphology of Mo-edge sites and the catalytic activity of other edge sites in 2H-MoS_2 are discussed. The Tafel slope and exchange current density of experimental catalysts for HER are compared to determine their relative performance.

The fundamental theory of semiconductor photoelectrochemistry is discussed primarily in qualitative terms with some quantitative relationships. The concepts of the depletion region, band bending, quasi-Fermi levels, and photocurrent are all discussed to provide insight into the forthcoming experimental results. Device design considerations with respect to protective layers and buried p/n+ junctions are discussed with summaries of recent progresses in literature. The following chapters will describe a laboratory effort to nanostructure MoS_2 on p-Si substrate for applications as a photocathode for HER. Colloidal lithography was used to pattern nanodisks of MoS_2 on the surface of p-Si using successive coating, e-beam deposition, oxygen plasma etching, and chemical etching steps. The performance of bare p-Si and MoS_2/p-Si was tested under solar irradiation in a custom-made PEC cell. These results are discussed in the context of the preceding theory, and plans for future work are outlined.

CHAPTER 2. Fabrication of MoS_2 nanodisks

Colloidal lithography was used to pattern MoS_2 nanodisks at varying densities on the surface of p-Si for applications in photoelectrochemical hydrogen evolution. Using a combination of layer-by-layer polyelectrolyte self-assembly, spin-coating, immersion coating, and self-assembled monolayers of polystyrene latex (PS) spheres, increasing densities of patterns of were created and analyzed using ImageJ. The density of PS spheres ranges from 4.7% coverage and .96 μm/μm^2 edge length density for the lowest concentration spin-coating procedure to 21% coverage and 3.95 μm/μm^2 for the immersion coating procedure. Then, the patterns were transferred to disks of MoS_2 using spin-coated polymer films, e-beam deposition, reactive oxygen plasma, and development in organic solvent. Brief exposure (3s) to reactive oxygen plasma was used modify the hydrophilicity of poly(methyl methacrylate) (PMMA) film for the immersion coating of PS spheres. Microposit S1811 was also explored because of its hydrophilicity, but the coating thickness could not be reduced below 1 μm. The resulting patterns of MoS_2 from the immersion coating of 500 nm PS spheres had a median disk diameter of 446 nm (calculated from area), a coverage of 21%, and an edge length density of 2.0 μm/μm^2. Furthermore, the thickness of Mo deposited via e-beam was used to control the thickness of the MoS_2 nanodisks. Atomic force microscopy characterization of these MoS_2 nanodisks reveals that the thickness ranges from 1.0–2.5 nm for MoS_2 grown from 1 nm Mo and 8.0–9.5 nm grown from 4 nm Mo.

2.1 Methods

2.1.1 Layer-by-layer polymer electrolyte self-assembly on PMMA/p-Si

p-Si wafers (University Wafer, 1–10 cm, <100> SSP 500 μm) were cut into 1 in^2 squares and submerged successively in acetone, isopropanol, and deionized (DI) water for 5 min each in a sonicator. The p-Si chips were then rinsed with DI water and dried with a stream of pressurized nitrogen (N_2). The samples were pre-baked for 5 min at 180°C and allowed to cool to room temperature. An excess of poly(methyl methacrylate) (PMMA) (MicroChem, 495 A4) was added to the samples in a spin-coater (Laurell Technologies WS-650MZ-23), and the samples were spun at 500 RPM for 10s and 4000 RPM for 30s to produce ~200 nm films of PMMA. The samples were post-baked for 90 s at 180°C on a hotplate. Samples coated with Microposit S1811 were post-baked for 60 s at 115°C. Diluted solutions of S1811 were created with ethyl acetate.

The layer-by-layer (LbL) self-assembly of charged polymers and electrolytes provides a cheap and simple pathway to functionalize the surface of a substrate.[16] When the substrate is submerged in an aqueous solution of the polyelectrolyte, a thin film (2–6 Å) of the charged polymer self-assembles on the surface. When repeated with alternative charges, a static charge builds up on the substrate, which affects wettability and affinity for charged nanoparticles. In this process, successive coatings of 4% poly(diallyldimethylammonium chloride) (PDDA), 4% polystyrene sulfonate (PSS), and 10% aluminum chlorohydrate (ACH) were used to increase the wettability of the surface and to build a static charge opposite the zeta potential of the polystyrene (PS) nanospheres. This process was carrier out on p-Si wafers coated with PMMA described above. Conditions for LbL self-assembly are summarized below in Table 1. A schematic illustration of the process can be found in Figure 6A. Between each step, the samples were rinsed with excess DI water and dried at an angle under a stream of pressurized

N_2. The samples were handled with tweezers held at a constant corner, and the stream was blown away from the tweezers to prevent contamination.

Table 1: Conditions for coating of PS nanospheres

Layer-by-layer coating of PS nanospheres		
Step	Solution	Duration
1.*	O_2 plasma	3 s
2.	4% PDDA	1 min
3.	4% PSS	1 min
4.	10% ACH	1 min
5.+	0.02 or 0.04 wt% PS in EtOH	10 s @ 500, 30 s @ 1000 RPM
6.*	0.25 wt% PS in H_2O	2 min
7.*	Boiling DI water	1 min

* Steps only required for immersion coating, + Steps only required for spin-coating

2.1.2 Spin and immersion coating

To generate low densities of spheres on the surface of PMMA/Si substrate, after the 3-layer polyelectrolyte self-assembly process, the substrates were loaded into a spin-coater and 50 μL of a solution of PS styrene spheres in ethanol was injected onto the surface of the substrate. After rotating for 10s at 500 RPM, the speed increased to 1000 RPM for 30s. Ethanol, which is less polar and more volatile than water was used to generate more uniform coatings. The first 10s at 500 RPM allow the solution to wet the substrate, and increasing the speed to 1000 RPM for 30s evaporates the solvent and distributes the spheres.[21] Increasing the

concentration of spheres in the initial solution, therefore, should result in denser coatings on the substrate. The parameters for this process are shown in Table 1. The wt% of PS nanospheres in the solution in Step 4 was modified between 0.004 and 0.02 wt%. A schematic of the spin coating process is shown in Figure 6A (right, top).

To generate higher densities of spheres on the surface of PMMA/Si substrate, the sample was submerged in a high concentration of PS nanospheres solution for 2 min. First, however, the surface of the PMMA must be altered by oxygen plasma for ~3 s increase the hydrophilicity of the film.[20] Various combinations of the LbL procedure shown in Table 1 were attempted throughout the process to optimize the hydrophilicity of the surface. A schematic of the immersion coating process is shown in Figure 6A (right, middle).

2.1.3 Self-assembled monolayer

To generate self-assembled monolayers, ~75 μL of 1:1 dilutions of PS nanospheres in ethanol were applied to the surface of water in Petri dish using a glass slide as an entrance ramp. Gradually, a monolayer of nanospheres formed on the surface of the water due to capillary forces and the evaporation of ethanol.[18] The SAM of nanospheres was then transferred to a PMMA coated p-Si substrate underneath the surface of the water, producing a hexagonally close-packed plane of spheres on the surface. This technique was use to create films of the maximum areal density. As the water level is lowered, the monolayers of spheres fall onto the substrate. The water was initially lowered using a transfer pipette. Then, when the SAM was close to the substrate, the sample was left to dry overnight. A schematic of the capillary forces between PS nanospheres floating on the surface of the fluid is shown in Figure 6A (right, top).

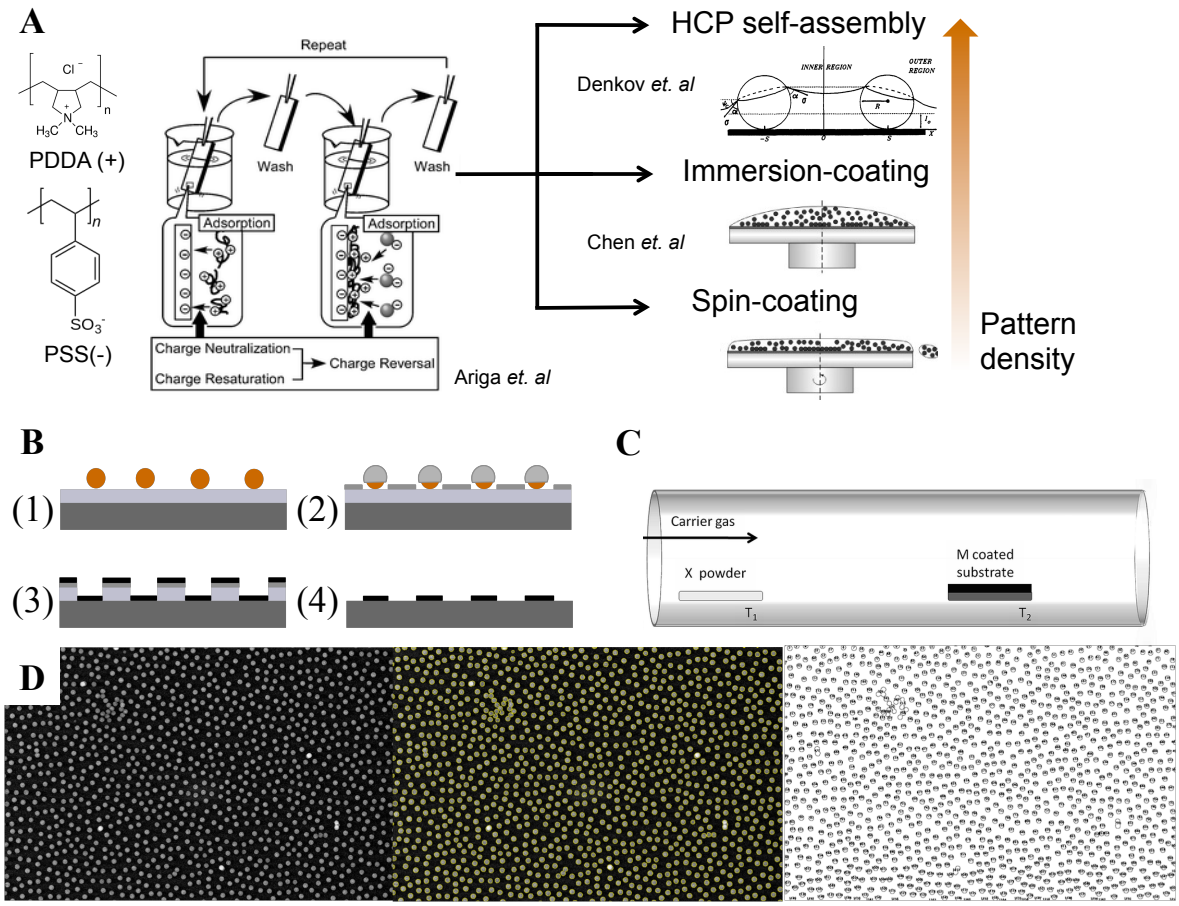

Figure 6: A: (left) Schematic of layer-by-layer polyelectrolyte coating process with monomers of PDDA and PSS. PMMA-coated p-Si were coated in layers of polyelectrolyte to modify the hydrophilicity and electrostatic potential of the surface (reproduced from Ariga *et. al.*[53]). (right) (top) Schematic showing capillary forces that pull together hexagonal close-packed (HCP) monolayers of PS nanospheres (reproduced from Denkov *et. al*[54]). (middle) Immersing LbL-coated PMMA/p-Si in 0.25 wt% PS solution coats spheres on the surface. (bottom) Spin coating PS spheres with controlled solution concentration allows for controlled pattern density (middle, bottom reproduced from Chen *et. al*[55]). **B:** Schematic of fabrication process. (1) PS spheres on PMMA/p-Si. (2) E-beam deposition of Cr (1 nm). (3) Removal of spheres and e-beam deposition of Mo (1 nm). (4) Dissolution of PMMA in acetone overnight leaves disks on Mo on surface.[56] **C:** Sulfur powder held at 110°C in temperature zone just outside furnace evaporates and is carried to the Mo-coated substrate by Ar. The sulfurization takes place at 550°C (reproduced from Bosi *et. al*[57]). **D:** Sample process flow for determining edge length density and fractional coverage from ImageJ. Left panel is original image, middle panel shows highlighted mask of particles over original image, and right shows the results of Particle Analysis.

2.1.4 Reactive ion etching and electron-beam deposition

First, 1 nm of Cr was deposited using the Cooke E-beam system to serve as a mask. This layer of Cr was on top of both the spheres and the PMMA. Adhesive tape was used to remove the layer of nanospheres on top of the polymer layer. In areas that were not covered by spheres, the Cr mask remained. But, in areas where the spheres were deposited and then removed, the PMMA layer was exposed. The samples were loaded into to March Plasma device and subjected to reactive oxygen plasma etching (RIE) for 2 min to remove the residual polymer layer. Then, 1 nm of Mo was deposited in the circular holes left by the spheres. Submerging the samples in organic solvent removed the PMMA layer, and the Cr mask was carried away, leaving only Mo disks on the p-Si substrate. This pattern transfer process is summarized below in Figure 6B.

2.1.5 Chemical vapor deposition

An excess (1 g) of solid sulfur was weighed and pushed into the open orifice on the right of the quartz glass tube on the chemical vapor deposition (CVD) furnace. At the left side of the quartz glass tube, the samples were loaded into a glass transfer boat that resembled a hollow half-cylinder. Using magnets on the interior and exterior of the boat, it was pushed into the middle of the heating furnace. First, quartz glass tube was evacuated to below 20 mTorr using a vacuum pump and manipulation of the gas manifold. The furnace was evacuated 3 times to remove any residual water vapor or oxygen. Then, 5 sccm of Ar was allowed to flow into the gas manifold. The temperature of the inside of the furnace was increased to 550°C and the temperature at the region of the quartz glass tube that contained the S was around 110°C. This temperature was hot enough to sublime the S powder, allowing it to be carried by the inert

gas stream to the sample. After reacting for 30 min, the heating furnace was turned off, and the temperature was allowed to decrease to room temperature under Ar flow for several hours. This process is shown schematically in Figure 6C.

2.2 Results and Discussion

2.2.1 Density variation of polystyrene nanospheres

Optical and scanning electron microscopy was used to characterize the edge length density (μm/μm^2) and fractional coverage of the (μm^2/μm^2) of the PS spheres on PMMA/p-Si. For an ideal pattern transfer process, these parameters would be represented in the resulting pattern of MoS_2 nanodisks on the p-Si. **Figure 7**A-C shows the density modification results for 200 nm (left) and 500 nm (right) PS spheres. For both series, the 0.004 wt% (Figure 7A) solution produces the lowest edge length density and fractional coverage, while the 0.25 wt% solution produces the highest (**Figure 7**D). Decreasing the solution concentration below 0.004 wt% led to aggregation of the spheres on the PMMA surface. For each of the samples shown in Figure 7, nine images were taken in 9 regions of the 1 in x 1 in sample. There is some variation in the density depending on the location of the image, but this variation was only significant near the edges. At the edges of the samples it was not uncommon to observe bands of aggregated spheres. For sample-to-sample comparison of optical microscope images, the image was taken as close to the center of the sample as possible. For SEM characterization, a small (~0.01 cm^2) piece of the Si was cleaved using a diamond scribe. The relationship between edge length and fractional coverage should be $\frac{2}{R_{PS}}$ where R_{PS} is the radius of the PS sphere. These results are shown in **Figure 7**D, where the dashed lines show the expected relationships. Any data below the dashed line, therefore, indicates a loss of measured edge length from

aggregation. Data above the dashed line represents an overestimation of perimeter from image processing. These results indicate that both the radius of the PS sphere and the method of coating are handles for density modification of the resulting MoS_2 patterns. The edge length density could be increased at a constant fractional coverage by decreasing the radius of the PS spheres. This analysis could be useful in further PEC hydrogen evolution experiments with patterns of MoS_2 nanodisks. The edge length density should have a direct linear relationship with the exchange current density, but the coverage will a competing, negative effect due to photoabsorption in the semiconductor layer.[14]

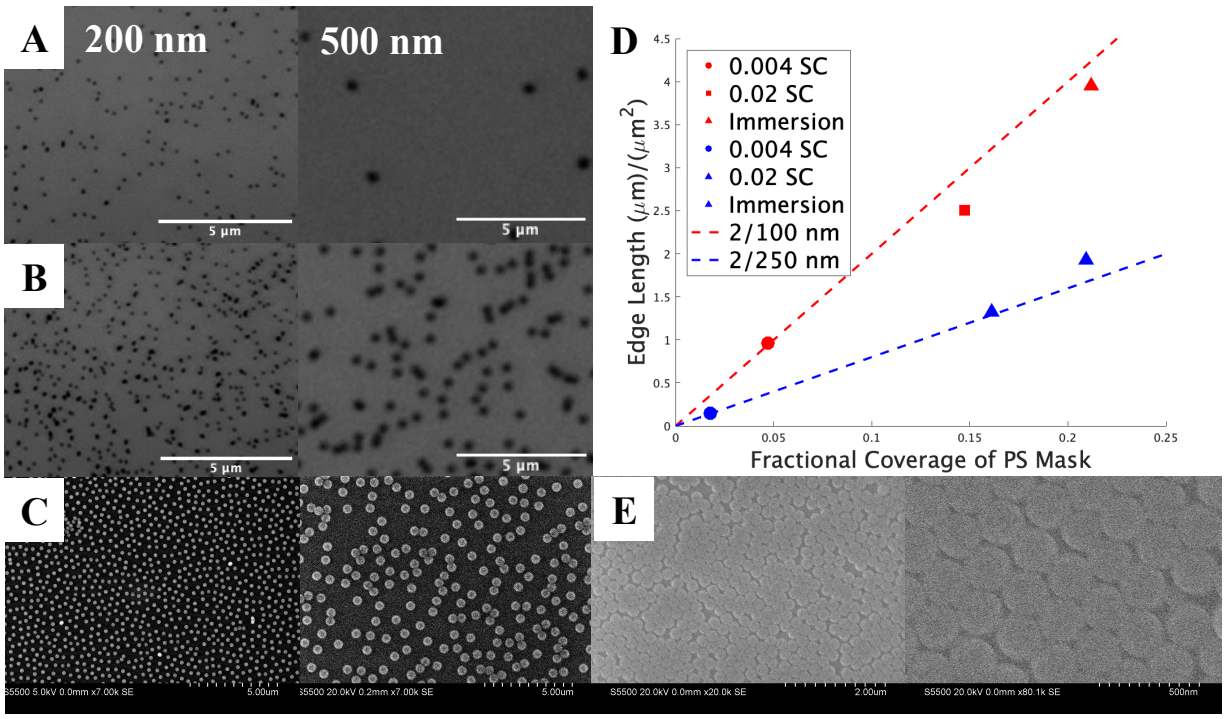

Figure 7: Density variation of PS spheres (200 nm, left; 500 nm right) on modified PMMA/p-Si **A:** Optical microscope image of 0.004 wt% PS in EtOH spin coat sample. **B:** Optical microscope image of 0.02 wt% PS in EtOH spin coat sample. **C:** SEM image of 0.25 wt% in DI H_2O immersion coat sample. **D:** Edge length density $\mu m/\mu m^2$ vs. Fractional coverage ($\mu m^2/\mu m^2$). Fit line shows relationship for ideal circles. Data below line represents loss of edge length from aggregation. **E:** SEM image of self-assembled monolayer on PMMA/p-Si.

Hexagonally close-packed (HCP) layers of PS nanospheres are shown in **Figure 7**E. Although MoS_2 patterns from HCP samples were not explored in this set of experiments, the long range order from close-packing can be utilized to create highly ordered catalyst patterns, as demonstrated by Ji and others.[58] The HCP patterns of spheres are subjected to an additional reactive ion etching step that etches away the top half of the sphere and a portion of the remaining bottom half. The diameter of the disk co-planar with the substrate depends on the time of RIE. This translates the long range order of the HCP patterns to the long range order of disks separated center-to-center by twice the initial diameter but with a tunable circumferential separation, allowing for an controlled optimization of the catalyst active area and surface coverage.

2.2.2 Pattern transfer process

After the layer-by-layer polyelectrolyte process, the surface of PMMA has an acceptable affinity for EtOH to permit spin coating of PS nanospheres. For the immersion coating samples, however, the surface chemistry of PMMA does not allow the a layer of PS spheres to form, even after several layer-by-layer polyelectrolyte coatings at increased concentrations and increased immersion times. For the immersion coating samples, therefore, it was necessary to explore other sacrificial polymer layers. Microposit S1811 photoresist was chosen because of the favorable hydrophilicity of the novolac resin polymer. As shown in **Figure 8**B, the films of S1811 were hydrophilic enough to create high density patterns of PS spheres via immersion coating after successive layer-by-layer polyelectrolyte build-up. The thickness of the film, however, could not be decreased below ~1.10 μm, even at 8000 RPM spin coating of the resist. Although reaction oxygen plasma etching is supposed to be anisotropic, at polymer resist thicknesses ~200 nm, as shown in **Figure 8**A, isotropic etching

began to remove polymer in areas covered by the Cr mask. It was then hypothesized that diluting the resist solution with molecule to similar structure to propylene glycol monomethyl ether acetate, which made up 70-80% of the resist solution, would result in more diluted, thinner films more amenable to anisotropic pattern transfer. Shown in **Figure 8**C-E, increasing the concentration of ethyl acetate in the resist solution from 0 wt% (right) to 2 wt% (middle) and 5 wt% (left) did not appreciably change the thickness of the resulting film. At concentrations above 5 wt%, the film coverage on the substrate was spotty and non-uniform.

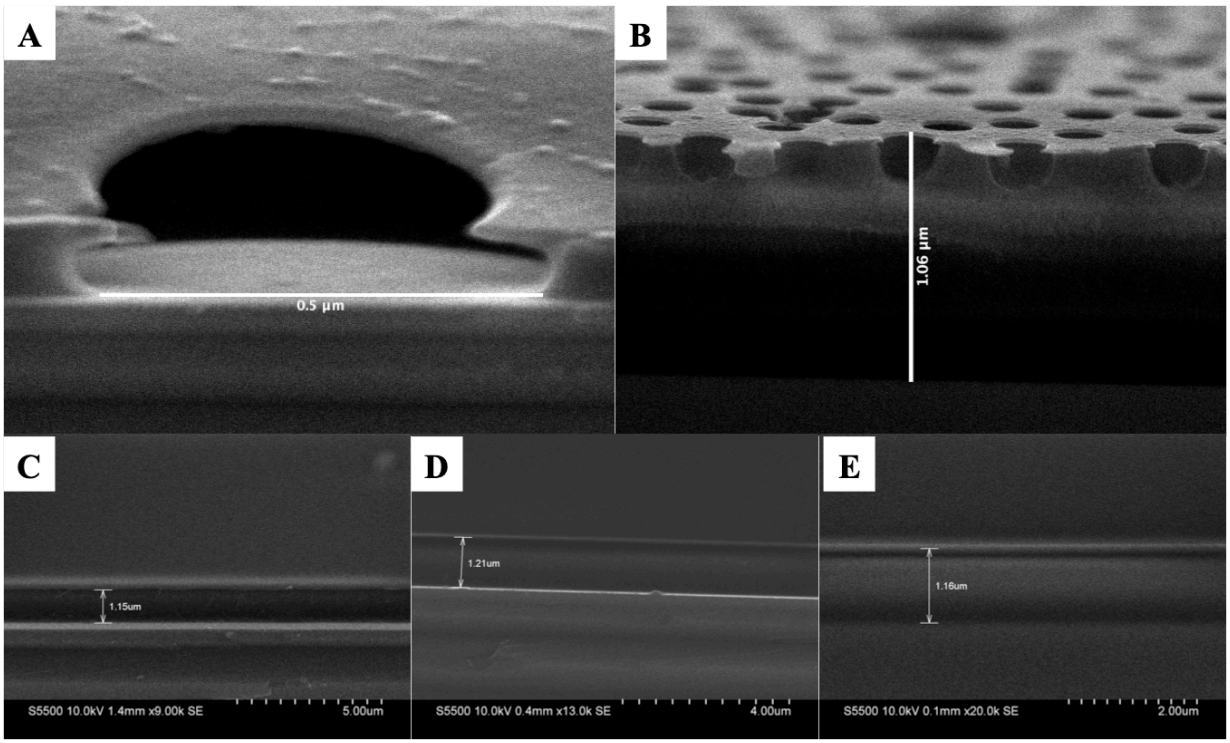

Figure 8: A: After 1 nm of Cr e-beam deposition and removal spheres, films were treated with reaction oxygen plasma for 2 min to remove 200 nm of PMMA via anisotropic etching. **B:** Films of S1811 resist provided desirable hydrophilicity but were too thick to be etched anisotropically. **C-E:** Dilution films of S1811 (C, 1.15 µm) with 2 wt% (D, 1.21 µm) and 5 wt% (E, 1.19 µm) did not have a significant effect on film thickness.

It has been shown previously that briefly exposing polymer films to reactive oxygen ion plasma creates negative surface charge and renders the surface more hydrophilic. Ng *et al*

showed that oxygen plasma replaced Si-CH_3 groups in poly(dimethylsiloxane) with Si-OH groups.[59] For this fabrication process, the films of PMMA on p-Si were exposed to 3s of reactive oxygen plasma before the LbL process and the immersion coating of PS nanospheres. It is hypothesized that the reaction ion plasma exposure replaced the two methyl groups in the repeating monomer of PMMA with hydroxyl groups, creating a more hydrophilic surface. This process modification successfully produced high density patterns of PS nanospheres on PMMA, as shown in **Figure 7**C.

2.2.3 MoS_2 nanodisks on p-Si substrate

After successive Cr deposition, PS nanosphere liftoff, Mo deposition, and sulfurization, MoS_2 nanodisks were formed on p-Si, as shown in **Figure 9** and **Figure 10**. Imaging software was used to find the distributions of area and perimeter, coverage, and edge length density. The MoS_2 nanodisks created from a mask of 500 nm PS nanospheres had a median area of 0.215 μm^2 and a median perimeter of 1.624 μm. The percent coverage was 18.2% with an edge length density of 1.18 $\mu m/\mu m^2$. The ratio of these two values is 6.5, which is 18.7% lower than the ideal ratio for perfect disks. This likely indicates a modest degree of agglomeration of spheres, as shown by the outlying perimeters and areas in **Figure 9**C-D. SEM images were also used to characterize 200 nm MoS_2 nanodisks (**Figure 10**). The 200 nm MoS_2 nanodisks had a median area of 0.053 μm^2 and a median perimeter of 1.146 μm. The percent coverage was 17.5% with an edge length density of 4.13 $\mu m/\mu m^2$. The ratio of these values is 23.7 which is 18.5% higher than the ratio for perfect disks. This indicates an overestimation of disk perimeter and/or an underestimation of disk area from image processing. But, 200 nm spheres provide patterns of MoS_2 with significantly increased edge length densities (4.13 vs. 1.18 $\mu m/\mu m^2$) at a relatively constant surface coverage (17.5% vs. 18.2%).

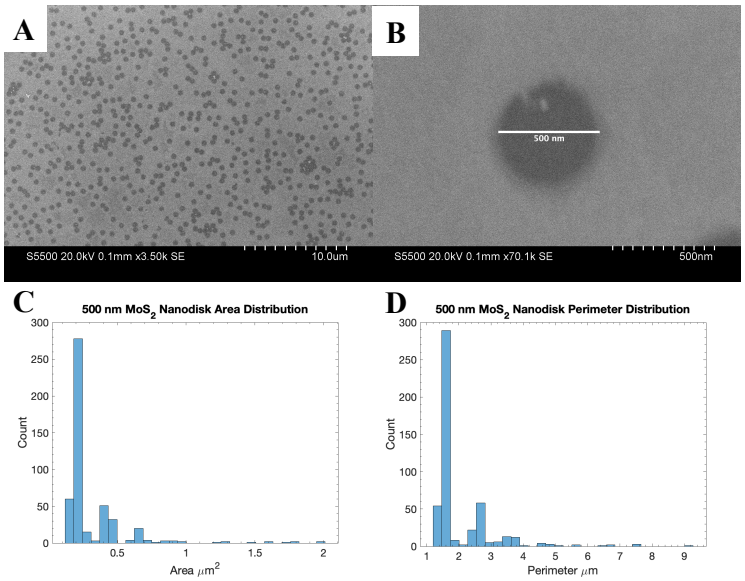

Figure 9: 500 nm MoS_2 nanodisks on p-Si. **A-B:** SEM images at low (left) and high (magnification) show the formation of MoS_2 disks on the surface. **C-D:** Imaging software was used to quantify the median area (0.215 μm^2) and the median perimeter (1.624 μm).

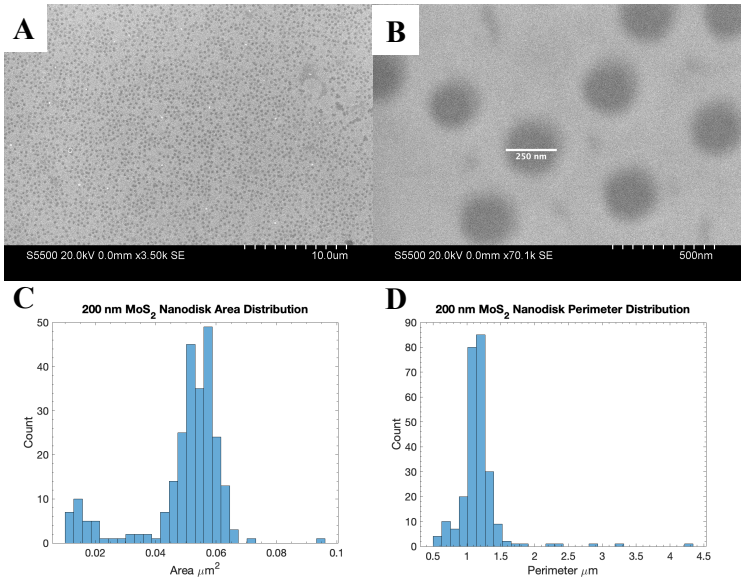

Figure 10: 200 nm MoS_2 nanodisks on p-Si. **A-B:** SEM images at low (left) and high (magnification) show the formation of MoS_2 disks on the surface. **C-D:** Imaging software was used to quantify the median area (0.053 μm^2) and the median perimeter (1.146 μm).

For the photoelectrochemical evolution of H_2 with active edge sites at the perimeters of the MoS_2 nanodisks, the 200 nm patterns, therefore, should show in activity relative to the 500 nm patterns commensurate with the increased edge length density. In future research, it may be possible to create similar patterns from even smaller spheres, allowing edge length density to be increased at a constant coverage.

Atomic force microscopy (AFM) was used to characterize the thickness of the MoS_2 nanodisks. The thickness of the Mo deposited via e-beam can be used to control the thickness of the resulting MoS_2. Two different thicknesses of Mo (1 nm and 4 nm) were both sulfurized for 200 and 500 nm patterns from immersion coating, creating the four samples shown in **Figure 11**. The red line represents the path taken by the AFM tip, and the blue circles are points of reference for comparison to the accompanying height profile. For 500 nm disks (**Figure 11**A-B) from 1 and 4 nm Mo, the height was approximately 1.5 nm and 8.0 nm, respectively. For 200 nm (**Figure 11**C-D) disks from 1 and 4 nm Mo, the height was approximately 2.5 nm and 8.5 nm, respectively. The differences in AFM profile for 200 and 500 nm samples grown from the same thickness of Mo may indicate different compositions of a- and c-domains of 2H-MoS_2.[45] In a-domains, the basal (001) plane is oriented horizontal to the substrate, exposing active HER sites only at the edges. However, for c-domains, the (001) planes are oriented orthogonally to the substrate, producing a higher density of active sites. Previous works have used high-resolution transmission electron microscopy (HRTEM) to investigate the thickness-dependence of the relative composition and a- and c-domains and suggested that thicker films had higher PEC activity because they had more vertically stacked c-domains.[45] Furthermore, it is possible that the kinetics of the sulfurization reaction determine

the preferred orientation of the 2H-MoS_2. This should be investigated in future work in order to determine the significance of non-circumferential edge sites.

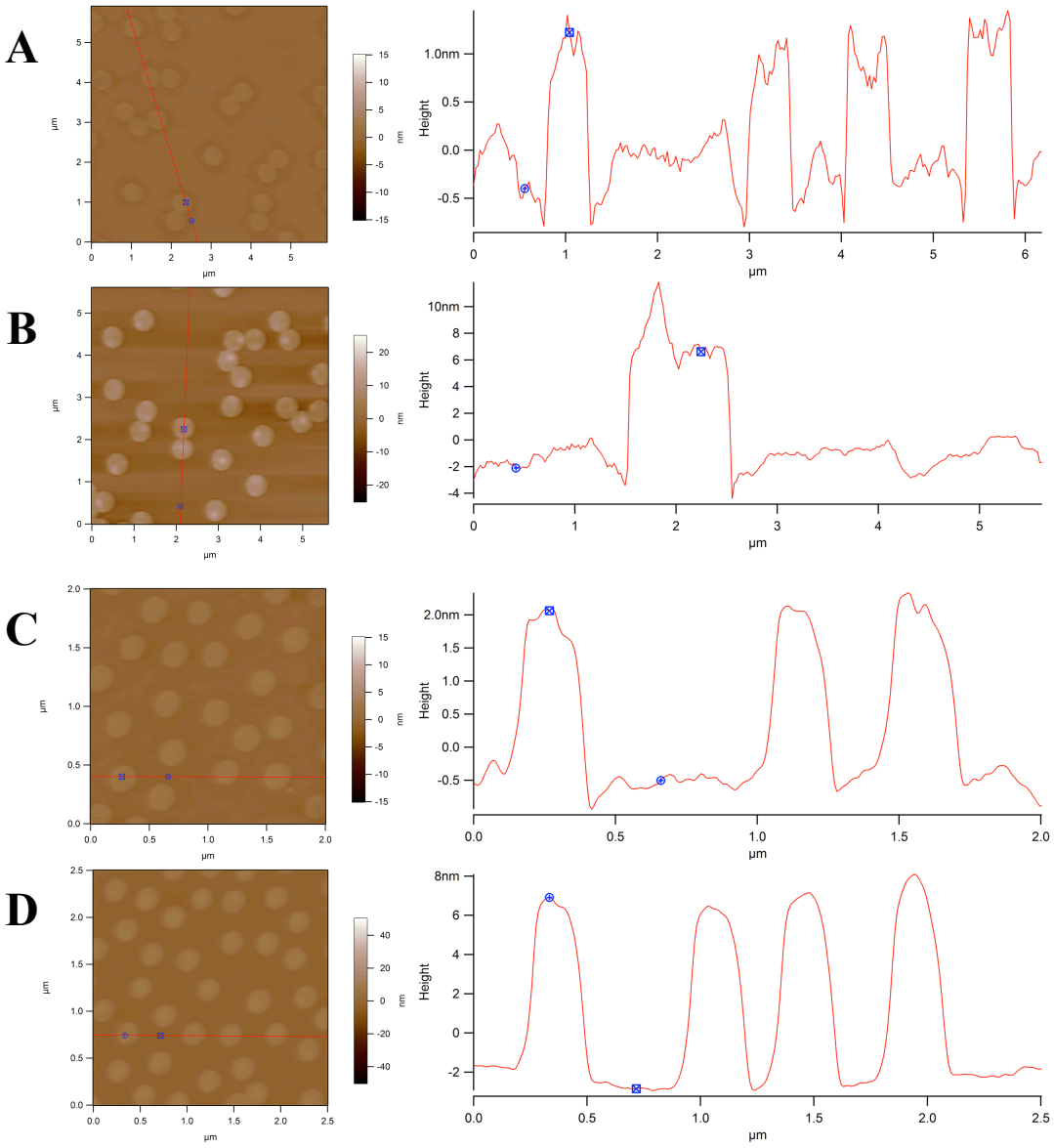

Figure 11: Atomic force microscopy characterization of MoS_2 nanodisks **A:** 500 nm from 1 nm Mo, z = 1.5 nm (distance between blue circles). **B:** 500 nm from 4 nm MoS, z = 8.0 nm. **C:** 200 nm from 1 nm Mo, z = 2.5 nm. **D:** 200 nm from 1 nm Mo, z = 9.5 nm.

The crystal structure of the MoS_2 nanodisks was verified using Raman spectroscopy. Typically, two characteristic absorption peaks are used to verify material as 2H-MoS_2, E^1_{2g} and

A_{1g}, which correspond to in-plane and out-of-plane vibrational modes, as illustrated in **Figure 12**.[26] Raman spectra were collected using continuous films of MoS_2 produced via the sulfurization of Mo in a procedure that replicated that used to sulfurize Mo disks. Two different films were analyzed with MoS_2 grown from 1 nm and 4 nm Mo. The absorption spectra were normalized and calibrated to the characteristic absorption peak of the silicon substrate at 520 cm^{-1}.[60] As the thickness of the MoS_2 film increases, the vibrational modes are expected to stiffen and spread apart in energy, and other groups have used the intensity ratio between the A_{1g} peak and the Si peak to compare the thickness of films.[61, 62] The characteristic absorptions for the continuous film from 1 nm Mo appear at 382.9 and 408.7 cm^{-1} for the E^1_{2g} and A_{1g} vibrational modes, respectively, which agrees well with previously reported data.[62] The absorptions for the continuous film from 4 nm Mo appear at 379.5 and 408.8 cm^{-1} for the E^1_{2g} and A_{1g}, respectively. The shift in absorption from 382.9 to 379.5 cm^{-1} indicates the increased thickness of the film and is consistent with previous reports.

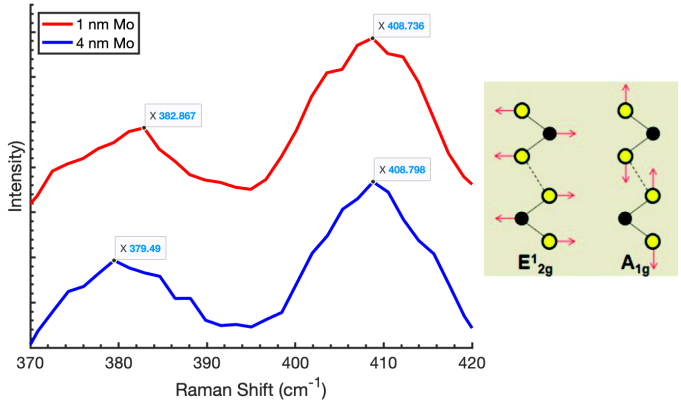

Figure 12: Raman spectra of continuous MoS_2 films produced from 1 and 4 nm Mo. The peaks at ~380 cm^{-1} and ~409 cm^{-1} correspond to the in-plane (E^1_{2g}) and out-of-plane (A_{1g}) vibrational modes, which are illustrated to the right.

2.3 Conclusions and Future Work

The goal of this research project was to use colloidal lithography to pattern MoS_2 nanodisks at varying densities on the surface of p-Si for applications in photoelectrochemical hydrogen reduction. Using a combination of layer-by-layer polyelectrolyte self-assembly, spin coating, immersion coating, and self-assembled monolayers of polystyrene latex (PS) spheres, increasing densities of patterns of were created and analyzed using ImageJ. The density of PS spheres ranges from 4.7% coverage and 0.96 $\mu m/\mu m^2$ edge length density for the lowest concentration spin-coating procedure with 500 nm spheres to 21% coverage and 3.95 $\mu m/\mu m^2$ for the immersion coating procedure with 200 nm spheres. Importantly, these procedures can be modified with commercially available nanospheres of varying sizes. Then, the patterns were transferred to disks of MoS_2 using spin-coated polymer films, e-beam deposition, reactive oxygen plasma, and development in organic solvent. Brief exposure (3 s) to reactive oxygen plasma was used modify the hydrophilicity of poly(methyl methacrylate) film for the immersion coating of PS spheres. Microposit S1811 was also explored because of its hydrophilicity, but the coating thickness could not be reduced below ~ 1 μm. The resulting patterns of MoS_2 from the immersion coating of 500 nm PS spheres had a median disk diameter of 446 nm (calculated from area), coverage of 21%, and an edge length density of 2.0 $\mu m/\mu m^2$. Atomic force microscopy characterization of these MoS_2 nanodisks reveals that the thickness ranges from 1.5 to 9.5 nm depending on the starting thickness of Mo.

Future work should involve further characterization of the MoS_2 nanodisks using x-ray photoelectron spectroscopy (XPS) and HRTEM to verify the expected stoichiometry and to investigation the relative composition of a- and c-domains in 2H-MoS_2. Improvements to the crystallinity and orientation of the MoS_2 monolayers may result from changes to the

sulfurization procedure, including synthesis temperature, temperature ramp rate, reactant concentration in carrier gas, and reaction time. Insights from photoelectrochemical testing of MoS_2 catalysts will dictate the optimal density, height, diameter, and orientation of 2H-MoS_2 to meet the desired application, and the insights gained from the fabrication procedures will allow us to fabricate bespoke catalyst patterns.

CHAPTER 3. Photoelectrochemical hydrogen evolution from p-Si and MoS_2

The purpose of this set of experiments was (1) to understand the fundamental mechanisms by which hydrogen evolves from the surface of p-Si in an electrochemical cell and (2) to compare the performance of p-Si without a catalyst coating with the the performance of optimized MoS_2/p-Si heterostructures. The key performance parameters in this context are the overpotential required to obtain -10 mA cm^{-2} in photocurrent; the stability of the photocathode for extended operation at one applied potential, *i.e.* chronoamperometry (CA), and for repeated linear potential scans, *i.e.* linear scan voltammetry (LSV); and the short-circuit (0.0V) current which represents hydrogen evolution without any electrical assistance. The methods and implications of the construction of the photoelectrochemical (PEC) cell are discussed along with the importance of the back electrical contact that connects p-Si to the external electrical circuit and potentiostat. The PEC performance and stability of bare p-Si are compared to heterostructures of continuous MoS_2 films and of MoS_2 nanodisks. Preliminary results suggest that 500 nm MoS_2 catalyst patterns from 4 nm Mo provide the best performance in terms of overpotential (-172 mV) and short-circuit current (-0.8 mA cm^{-2}) that future experiments are needed to resolve the discrepancy in performance between our reported continuous MoS_2 films and those discussed in relevant literature. The gradual decay in key performance parameters with LSV cylcing and extended CA operation identifies understanding and optimizing the growth of insulating surface oxide during PEC operation as a priority for future research. Growing thicker disks of MoS_2 via increased Mo deposition time represents a pathway for

performance enhancement, as suggested by recent literature. Finally, results from *in situ* observation of hydrogen evolution on the microscale are presented and applications for the precise light-driven manipulation of collodial nanomaterial are discussed.

3.1 Methods

3.1.1 Fabrication of photocathodes

In order to isolate the back electrical contact from the electrolyte solution, 3M (470) Electroplater's Tape was used to enclose the photocathodes.[63] A hole punch was used to produce a ~0.25 cm^2 hole in one piece of tape about 3" long and 2" wide. Si wafers (University Wafer, SSP, 1-10 Ω-cm, B-doped p-type, 500 μm) were cleaved into 1 cm^2 pieces and scratched on the unpolished side with a diamond scribe to remove the surface oxide layer. The scratched p-Si squares were placed on top of the hole on the adhesive side of the tape with the polished side showing through to the other side. To improve the contact between the p-Si and the wire, 10 μL Ga-In eutectic (Sigma-Aldrich, >99.99% trace metals basis) was painted onto the scratched Si surface. Insulated wire (Sparkfun, PRT-08023) was placed on the adhesive side of the tape with a small stripped portion placed on top of the Ga-In/p-Si. Alternatively, 20 nm of Au was grown via electron-beam evaporation (Cooke e-beam and Sputtering System) to create an ohmic contact, replacing Ga-In eutectic. Then, to adhere the wire to the surface, conductive two-part Ag epoxy (MG Chemicals, 83315-15G) was mixed in equal proportion and coated on the wire and Au/Si surface. After drying overnight, another piece of tape was placed on top of the Ag epoxy to complete the fabrication of the photocathode.

3.1.2 Three-electrode PEC testing

Before testing, the exposed, polished surfaces of the photocathodes were rinsed in DI H_2O and immersed in a 10 wt% HF aqueous solution for 120s to remove the native surface oxide layer. The samples were then immediately transferred to the custom-made PEC cell for testing. A custom-made cylindrical glass container was modified with a flat optical port on one side to create a planar optical path. The three-electrode set-up consisted of a Pt plate counter electrode, a Ag/AgCl reference electrode, and a photocathode. The photocathode was submerged in the aqueous electrolyte (0.5M H_2SO_4) and placed with the exposed surface in the planar optical path. For experiments in which the pH was manipulated, 1M H_3PO_4 0.5M Na_2SO_4 and 0.5M Na_2SO_4 were used to create pH = 1.66 and pH = 5.92 electrolytes, respectively. The placement of the photocathode was controlled to ensure that the p-Si surface was ~3 cm away from the flat ported window. The reference electrode was placed between the photocathode and the flat-ported window to allow for fast manipulation of electrolyte potential with respect to the Si surface. A solar simulator (Oriel LCS- 100 94011A) was calibrated to one sun (100 mW/cm^2) using a Newport 91150 V reference cell. For calibration, 3 cm of electrolyte were added to the bottom of the PEC cell and the cell was placed on top of the quartz window of the reference cell. A distance of 9.1 cm corresponded to one sun with 3 cm of electrolyte and one glass surface. For testing, the output of the solar simulator was placed 9.1 cm away from the flat-ported window of the PEC cell, recreating the calibration conditions. Linear scan voltammetry and chronoamperometry were conducted using a three-electrode potentiostat (VersaSTAT). The reported potentials vs. Ag/AgCl were converted as follows:

(1) V (RHE) = V (Ag/AgCl) + .197 V

3.1.3 Two-electrode PEC testing with optical microscope

A 0.254 cm^2 circular hole was cut into a thin (< 3 mm) layer of poly(dimethyl siloxane) (PDMS), and the resulting well was pressed onto the surface of p-Si with 20 nm Au back contact. This was attached to a glass slide using adhesive Cu tape and connected to a Keithley 2400 SourceMeter unit (SMU). A thin (~ 2 mm) strip of Pt was cut from Pt foil and inserted into the middle of PDMS well until the tip of the Pt was visible in the center of the well. The Pt foil was connected to the SMU using adhesive tape, and 50 μL of 0.5M H_2SO_4 was added to the center of the well. The surface of the p-Si was monitored with an optical microscope while the SMU swept the bias voltage to the two-electrode cell. This setup is shown in **Figure 20**.

3.1.4 Electrical characterization

A source meter (Keithley 2400) was programmed to sweep a bias voltage between -30 and 30 V with 1.05 compliance and a variable step size and time delay. One electrode was connected directly to the p-Si surface and the other electrode was attached a wire. The wire was attached to the surface via Ag epoxy or a combination of Ga-In eutectic and Ag epoxy. Analogous fabrication procedures were used to create Ag/Ga-In/p-Si and Ag/p-Si contacts. However, in this case, it was not necessary to enclose samples in tape.

3.2 Results and Discussion

3.2.1 Investigation of back-contact and bare p-Si I-V behavior

The testing of photocathodes first requires the appropriate design of a three-electrode set-up, and the selection of materials to create ohmic contacts between the p-type semiconductor and the electrical components of the potentiostat. Theoretically, an ohmic

contact between a Cu wire and p-Si requires the use of an intermediary metal with a work function greater than that of (100) p-Si (4.91 eV).[64] Of the common elements, only Au (5.31-5.47 eV), Ir (5.00-5.76), Co (4.53-5.10), and Pt (5.12-5.93 eV) meet these requirements, depending on the interfacial crystal facet.[65] For an ideal p-type semiconductor/metal junction, an accumulation region forms near the point of contact, as shown in **Figure 13**A.[66] If the work function of the metal back contact is lower than that of p-Si, a Schottky barrier forms that is equal to the difference in the work functions, and current only flows under positive bias. For the negative biases used in PEC testing, this limits hole extraction through the back contact and significantly reduces the photocurrent. Recent strategies have included creating an Al back contact using thermal evaporation.[67, 68] Heating a sample of Al/Si creates a highly Al-doped p^+ region near the contact with Al, which reduces the width of the depletion region associated with the Schottky barrier.[69] This narrow depletion region width allows holes to tunnel through the forbidden region, producing an ohmic contact. The prevailing experimental technique with p-Si, however, involves the use of Ga-In eutectic, a liquid metal alloy at room temperature, to facilitate the extraction of holes from the valence band of p-Si to open states in the metal wire.[45, 52, 70, 71] The reported work functions of Ga (4.31 eV) and In (4.09 eV), however, are below that required to create an ohmic contact with p-Si,[65] and the cost of the material, ~$15/gram, does not make the device amenable to large-scale manufacturing. Indeed, the motivating factor for the use of MoS_2 instead of Pt is removing rare metals from the manufacturing process.

In this work, p-Si photocathodes were fabricated and tested with and without the use of Ga-In eutectic. As shown below in **Figure 13**B, when only two-part Ag epoxy is used as a back contact for a bare p-Si photocathode, the current of the device reaches on -70 $\mu A/cm^{-2}$ at -

1.0 V vs. RHE under 100 mW/cm^2 AM 1.5 G irradiation, which is only 2.8x the dark current at the same voltage. The difference between the dark and light current at -1.0 V is shown again in the chronoamperogram (CA) in **Figure 13**C, which shows that manually shuttering of the light source produces a step change in the measured photocurrent. In this case, the measured current does not appear to be the result of a thermodynamic driving force induced by photoabsorption. In dark conditions, the reaction is thermodynamically favorable at very low currents; the light absorption simply provides the minority carriers to participate in the cathodic reaction. There does not appear to be effective separation of photogenerated holes and electrons, and the increase in the electrochemical reaction rate is, therefore, only the result of Δn, the number of photogenerated electrons in the conduction band.[72] As the current-voltage data in **Figure 13**D shows, the Ag epoxy back contact produces a Schottky barrier and the device behaves like a Schottky diode under negative bias.

When Ga-In eutectic is applied between the Ag epoxy and the p-Si, however, the measured current at -1.0 V vs. RHE under one sun is around -30 mA/cm^2 which is ~1500x more than the value without Ga-In eutectic (**Figure 13**E). Beyond -1.0 V vs. RHE the current is diffusion-limited, which means that the reaction consumes H^+ in solution faster than the protons can diffuse to the surface. The variation in the currents between the two samples at -1.0 V vs. RHE is due to the formation and removal of bubbles of hydrogen gas. When the local concentration of H_2 exceeds the saturation limit for the electrolyte, a gas bubble forms on the surface of the electrode.[73] This gas bubble blocks additional protons from reacting on that region of the electrode, and the current decreases. When the bubble increases and size and, eventually, floats to the surface of the liquid, it exposes the part of the electrode that was previously blocked, increasing the local reaction rate. Because of the small size of the

photocathode (~0.25 cm^2), the formation of bubbles has an appreciable effect on the measured photocurrent.[74] The dark current at -1.0 V for samples with Ga-In eutectic remains similar to that measured without the eutectic (~20-30 $\mu A/cm^{-2}$ at -1.0 V vs. RHE), which indicates that the separation of electrons and holes provides the thermodynamic driving force for the increased reaction rate. This is again reflected in **Figure 13**D, which shows that the Ga-In eutectic allows more current to pass at a negative bias. The overall behavior, however, largely resembles that of a Schottky diode. This increased conductivity at negative bias is most likely the source of the observed performance enhancements, but the contact is not ohmic. Ga and In are both p-type dopants of Si, and both form eutectics with very low concentrations of Si.[75] Below 29.7°C a Ga-Si eutectic forms with 0.006% Si. Similarly, below 156.8°C a In-Si eutectic forms with 0.004% Si.[76] It is possible that a Ga-In-Si eutectic helps to mediate hole extraction or that highly doped p^+ regions allow holes to tunnel through the Schottky barrier.

In order to remove the Schottky barrier between the wire and the p-Si photocathode, 20 nm of Au was deposited with e-beam evaporation on the back surface. The results in **Figure 13**E show that removing the barrier for hole extraction decreases the magnitude of the overpotential, defined as the potential at which the current exceeds -10 mA/cm^{-2}, from -593 mV for Ga-In/p-Si to -390 mV for Au/p-Si. This measured behavior of bare p-Si with Ga-In eutectic back contact is consistent with the reported data for PEC testing cells with 0.5M H_2SO_4 electrolytes,[45, 47, 52] but it differs from data reported with 1M $HClO_4$ electrolyte, which seems to have a lower overpotential.[51, 70, 71] Ji *et al* used similar e-beam methods to manufacture a 100nm Au back contact but only reported data for a p-Si/$SrTiO_3$ system, which showed a current of 2 $\mu A/cm^{-2}$ at -0.6 V vs RHE.[58] Other groups have used Au back contacts but have used different testing conditions not suitable for comparison.[77]

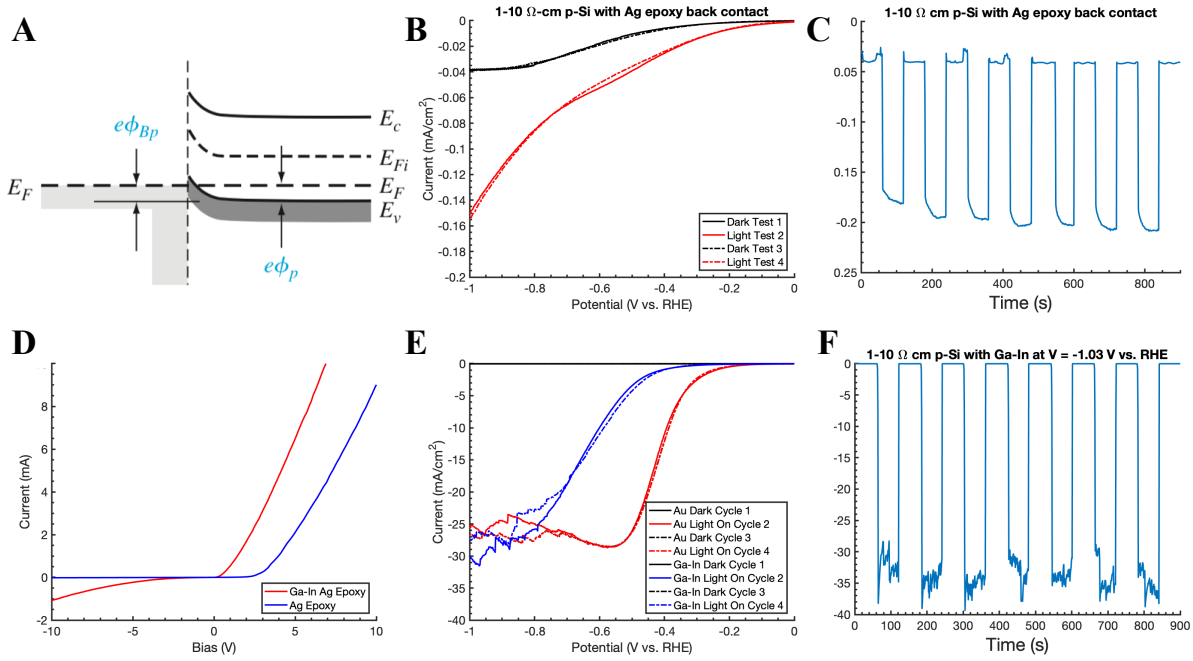

Figure 13: A: Ideal, ohmic, metal-semiconductor junction with accumulation region of height $e\phi_{Bp}$.[66] **B:** LSV for two-part Ag-epoxy back contact with bare p-Si. **C:** CA with manual shuttering of light at -1.0 V vs. RHE. **D:** Voltage sweeps of Ag epoxy and Ga-In eutectic back contacts show Schottky diode behavior at negative bias. **E:** LSVs for bare p-Si with Ga-In eutectic back contact (blue) and 20nm Au back contact (red). Au removes Schottky barrier and improves performance. **F:** CA with manual shuttering (every 1 min) shows stable current for 15 min.

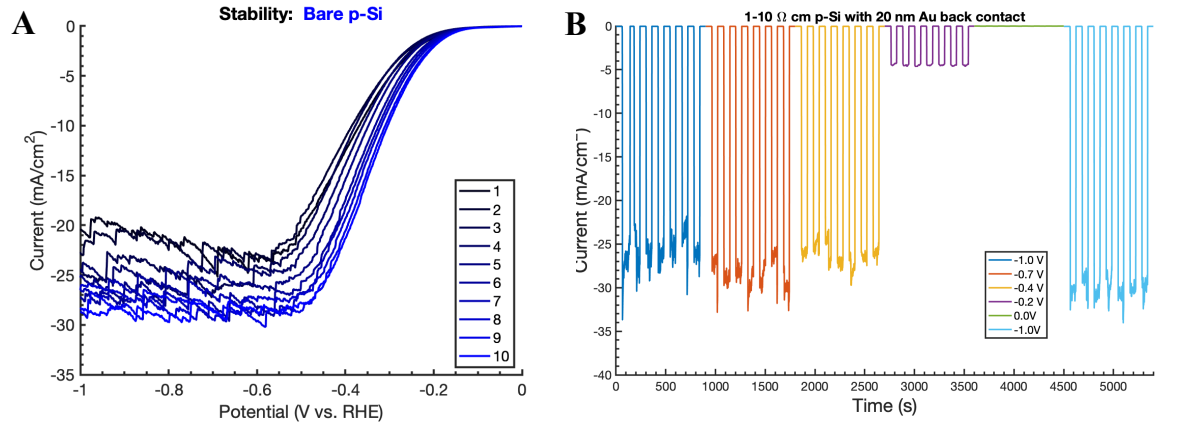

Figure 14: A: Successively linear scans of bare p-Si show monotonic increase in performance with each scan. **B:** Extended chronoamperometry at varying potentials to investigate mechanism of photooxidation. A slight increase in current is observed after returning -1.0 V vs. RHE after 1h 15 min of continuous testing.

The stability of Au/p-Si system was also investigated (**Figure 14**). Before testing, the bare p-Si photocathodes were immersed a solution 10% HF for 2 min to remove the surface oxide layer and to terminate the surface with Si-H bonds. During operation at -1.0 V vs. RHE the photocathodes are stable for at least 15 min without a measurable decay in photocurrent. This result differs from recent works that report immediate decay in photocurrent from bare p-Si during surface oxide layer growth. For this reason, it is common for researchers to grow an insulator layer between the p-Si semiconductor and the electrolyte. Ideally, this thin layer prevents electron-hole recombination via surface states, stops the growth of SiO_2, and allows tunneling of photogenerated electrons to a catalyst or to the electrolyte. However, in a recent report Choi, *et al.* found that the photocurrent from bare p-Si remained stable for 6 hr without the use of an Al_2O_3 insulator layer.[48] **Figure 14** shows the result of extended testing of bare p-Si at different voltages. It was initially hypothesized that operation at voltages closer to 0.0 V vs. RHE would be more favorable for the growth of SiO_2, so tests were carried out for 15 min at a range of potentials between -1.0 V and 0.0 V vs. RHE. The light source was manually shuttered in 1 min intervals, and the current oscillates between dark and light values depending on the voltage. The current values in **Figure 14** map well onto the current values reported in **Figure 13**E, and the current at 0.0V was approximately -10 $\mu A/cm^{-2}$ under illumination. After 1 hr of testing under a variety of applied potentials, the illuminated photocurrent at -1.0 V vs. RHE actually slightly increased (-29–32 vs. -25–28 mA/cm^{-2}) compared to the start of testing. This result, therefore, does not provide evidence for the growth of parasitic SiO_2. However, this result should be the focus of future work, as will be discussed in later sections.

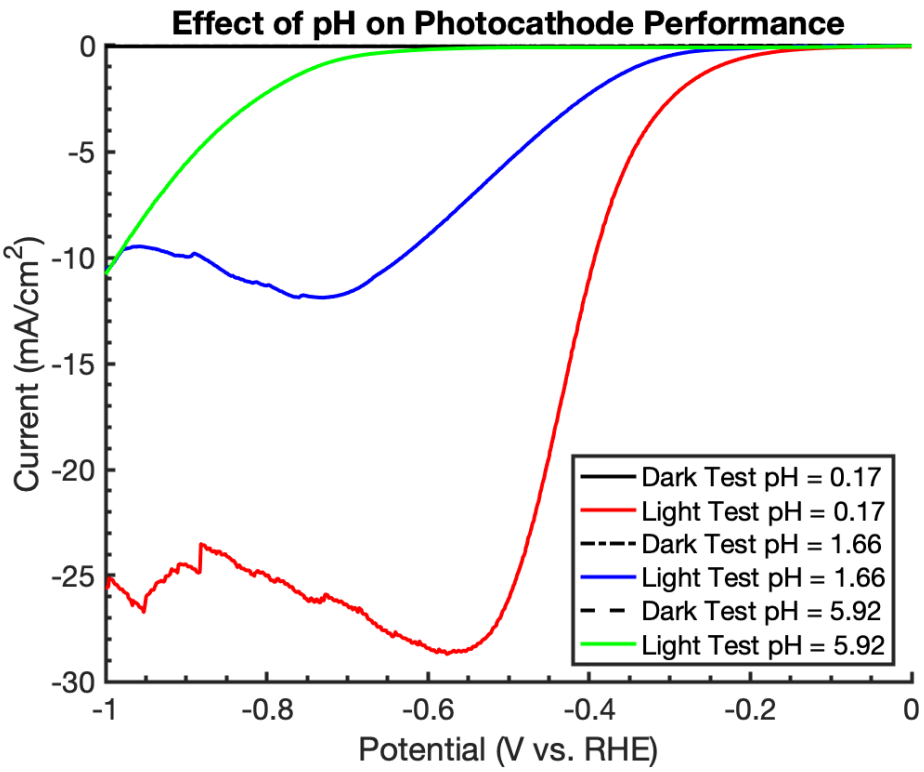

Figure 15: Performance of bare p-Si photocathode. Overpotential at -10 mA cm^{-2} decreases from -391 mV for 0.5M H_2SO_4 to -632 and -987 for 0.1M H_3PO_4 0.5M Na_2SO_4 and 0.5M Na_2SO_4, respectively.

The effect of pH on photocathode performance was also investigated (**Figure 15**). An electrolyte with pH = 1.66 was created with 0.1M H_3PO_4, a weak, triprotic acid and 0.5M Na_2SO_4 as supporting electrolyte. Additionally, an electrolyte with pH = 5.92 was created with only 0.5M H_2SO_4. The overpotential on bare p-Si increased in magnitude from -390 mV at 0.5M H_2SO_4 to -632 and -987 mV for the pH = 1.66 and pH = 5.92 solutions, respectively. For practical implementation, the stability and performance of photocathodes in weakly acidic or neutral conditions could decrease the overall carbon footprint of the energy conversion process and allow for operation using natural bodies of water. pH dependence is likely to be weaker once MoS_2 is added to the surface of p-Si; Morales-Guio, *et al.* found only a slight decrease in the photocathode performance of MoS_{2+x}/p-CuO_2 when the pH was increased from 1 to 4.

Furthermore, the authors found that the loading of the catalyst could be increased to offset current losses.[78] The stability of Si in harsh, acidic conditions allows for the use of low pH (≈0) electrolytes, but when CdS, CdSe, or Cu_2O are used as photoabsorbers, researchers often run PEC tests in electrolytes ranging from pH 1 to 7, as summarized in a recent review paper.[79]

3.2.2 PEC from continuous MoS_2 and MoS_2 nanodisks

The PEC performance of continuous films of MoS_2 grown via direct sulfurization shows insignificant photoabsorption in the underlying p-Si. The fabrication for continuous films of MoS_2, discussed earlier, involved the exact same Mo e-beam deposition and sulfurization steps, but, without colloidal lithography, a thin film of Mo (1–4 nm) was allowed to grow in a continuous layer without exposing p-Si to the electrolyte. The overpotential at -10 mA cm^{-2} was -721 mV for the continuous film fabricated from 4 nm of Mo. These surprising results (**Figure 16**) possibly indicate the tradeoff discussed in the fabrication section between available active sites for HER—edge length density ($\mu m/\mu m^2$)—and coverage (%) of the underlying semiconductor, which was hypothesized to result in decreased light absorption efficiency. Similar studies of MoS_2/p-Si heterojunctions, however, have reported significant photoabsorption in continuous film heterojunctions fabrication with a variety of methods. Benck *et al.* grew ~3.6 nm of Mo on n^+-p-Si with magnetron sputtering and sulfurized the continuous films with a mixed source of H_2/H_2S.[80] Cross-sectional transmission electron microscopy images showed the presence of both an underlying, un-sulfurized Mo layer and MoSi composite layer. PEC testing relative to dark controls revealed that surface coatings only decreased absorption ~10% compared to bare n^+-p-Si. Although this reported sulfurization procedure differs slightly, the direct sulfurization of Mo matches our fabrication procedure and provides the best estimate for the optical properties we can expect from out photocathodes.

Others have reported the optical absorption of MoS_2 films transferred to SiO_2 and found that the absorption varies with MoS_2 thickness from ~4% for 4 nm MoS_2 to ~78% for 29 nm MoS_2.[45] Ding *et al*. fabricated films of MoS_2 with thicknesses on the nanoscale via CVD and drop-casting and reported hydrogen evolution at short-circuit voltage.[81] Similarly, Joe *et al.* fabricated Cl-rich MoS_2 films on p-Si using several hundred atomic layer deposition (ALD) cycles and obtained PEC performance comparable to other reports.[52] Thus, although Raman spectroscopy results (**Figure 12**) confirm the presence of 2H-MoS_2 in these continuous film samples, this result needs to be investigated further to address disagreement with literature reports.

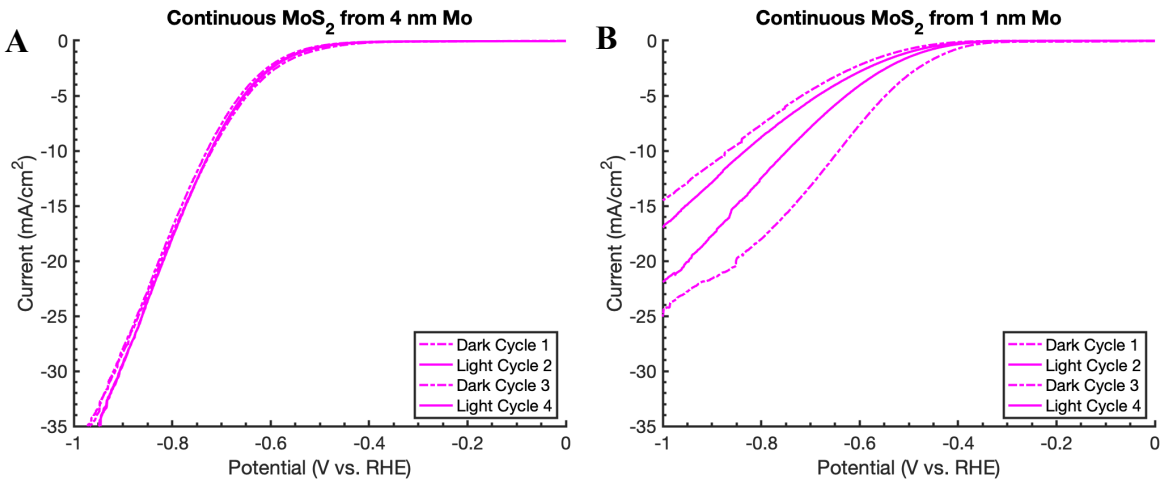

Figure 16: A: Continuous film from 4 nm Mo shows stable electrocatalyic current without semiconductor photoabsorption. **B:** Continuous film from 1 nm Mo shows decay in current with successive cycling.

The difference in stability and current, however, between films fabricated using 4 nm and 1 nm Mo, however, does reveal the influence of thickness on PEC performance. After cycles alternative between dark and light, the continuous film fabricated from 4 nm Mo showed no appreciable decrease in current while the sample fabricated from 1 nm Mo showed

an increase in the magnitude of overpotential at -10 mA cm^{-2} from -642 to -832 mV. The decrease in performance between the first and fourth cycles for the continuous film fabricated from 1 nm Mo suggests either a change in chemical composition of the photocathode surface or the delamination of the catalyst layer. The effect of thickness of the stability of photocathode heterojunctions is consistent with those obtained for MoS_2 nanodisk samples, discussed later.

The current-potential behavior of p-Si was compared to those of the MoS_2/p-Si heterojunctions with 200 nm and 500 nm disk catalyst patterns. Each catalyst pattern was made using immersion coating of PS spheres with an e-beam Mo thickness of 4 nm. In contrast to bare p-Si, both 200 nm and 500 nm MoS_2/p-Si showed a marked decrease in performance after 10 linear potential scans. As shown in **Figure 17**A, at less negative applied potentials the performance of the 500 nm MoS_2 was superior to that of the bare p-Si, although the performance decreased with each successive cycle. Defined as the potential at which the current passed -10 mA cm^{-2} and recorded for the first LSV, the overpotentials for 200 and 500 nm MoS_2 nanodisk patterns produced via immersion coating were -234 and -172 mV, respectively, compared to -390 mV for bare p-Si. However, after ten cycles the magnitudes of the overpotentials for 200 and 500 nm MoS_2 increased to -377 and -218 mV, respectively, and the magnitude of the overpotential for bare p-Si decreased to -305 mV. As shown in **Figure 17**B, the performance of bare p-Si begins to eclipse that of 200 nm MoS_2 after several cycles. The smallest overpotential (-172 mV) belongs to the 500 nm MoS_2 nanodisk pattern, which does not provide evidence for the linear dependence of exchange current on the circumferential edge length density. The percent coverages of the 200 and 500 nm immersion coating samples are nearly equal (~18%) but the 200 nm sample had nearly 4x (4.14 vs. 1.18 $\mu m/\mu m^2$) the

circumferential edges per unit area. As discussed in the fabrication portion of this report, the performance enhancement from increased circumferential edges may have been outstripped by the enhancement from vertical c-domains in the 500 nm samples. The confined growth area for 200 nm MoS_2 may have preferentially exposed basal places, while the 500 nm growth area exposed vertically stacked Mo-edges. This hypothesis could be tested with high-resolution transmission electron microscopy (HRTEM) images of the samples.

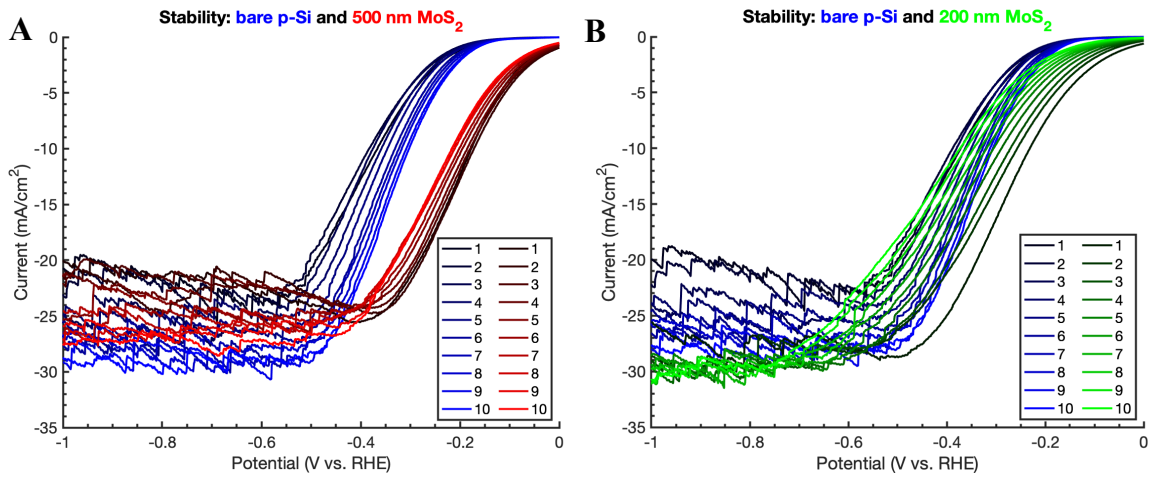

Figure 17: Comparison between bare p-Si and MoS_2/p-Si from immersion coating and 4 nm Mo. **A:** 500 nm MoS_2 nanodisks show performance enhancements despite decrease in performance with successive cycling. **B:** 200 nm MoS_2 nanodisks show initially performance enhancement, but perform worse than p-Si after successive potential scans.

Still, the most important performance parameter for photoelectrochemical hydrogen evolution catalysts is the short-circuit current, *i.e.* the current without applied potential. The current from the electrocatalytic evolution of hydrogen from Pt foil increases exponentially at voltages more negative that 0.0V with an overpotential at approximately -40 mA cm^{-2} of -100 mV.[28] Thus, the simply conversion of electric to chemical energy is possible with high efficiencies using precious metal catalysts. PEC conversion allows for solar energy to be

converted at short-circuit potential or at positive, anodic potentials, and, thus, represents a pathway by which the solar energy can be converted without electrical assistance.

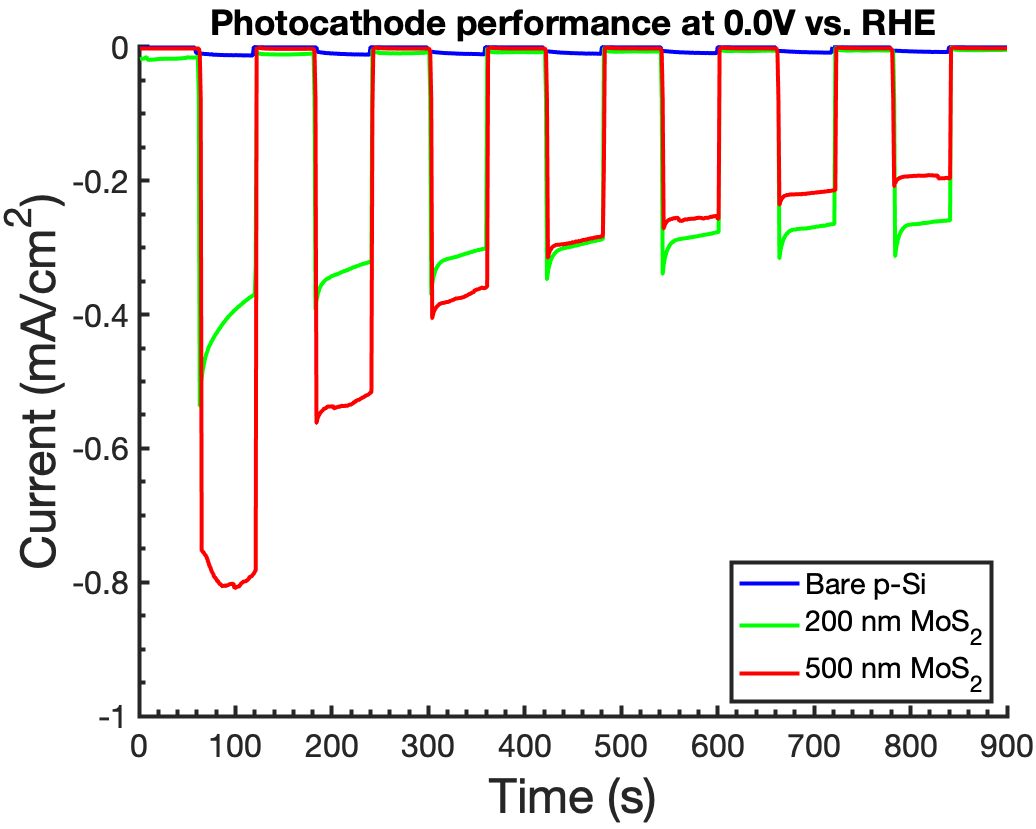

Figure 18: Short-circuit performance comparison of bare p-Si/, 200 nm MoS_2/p-Si and 500 nm/p-Si.

The results of the short-circuit testing of the 200 and 500 nm MoS_2 patterns are shown in **Figure 18**. The solar simulator was manually shuttered on a 1 min time interval, and the dark/light currents show a clear on/off behavior. Within the 15 min testing period, the light current for bare p-Si decreased from -13 to -7.5 μA cm^{-2} while the dark current remained stable at -0.5 μA cm^{-2}. The 500 nm MoS_2/p-Si pattern initially showed the best performance at -0.80 mA cm^{-2} but decreased to -0.2 mA cm^{-2} by the end of the test. Similarly, the 200 nm MoS_2/p-Si initially showed a -0.45 mA cm^{-2} current under illumination but decayed to -0.26 mA cm^{-2}. The

dark current for 500 nm MoS_2/p-Si remained relatively stable at around -2.0 μA $cm^{-2.}$ while the dark current for 200 nm MoS_2/p-Si decreased from -15 to -5 μA cm^{-2}.

Compared to relevant literature results, the short-circuit currents and measured overpotentials for MoS_2/p-Si heterojunction catalysts need improvement. Defined as the potential at a current of -10 mA cm^{-2}, the overpotential for state-of-the-art MoS_2/p-Si photocathodes has been reported to be around +0.160 V vs. RHE, with saturated, diffusion-limited currents as a high as -37 mA cm^{-2} at short-circuit voltage. By contrast, the best recorded data in this work shows an overpotential of -0.172 V and a temporary short-circuit current of -0.80 mA cm^{-2}. Still, these results match well with preliminary results reported for state-of-the-art systems. For example, the photocurrents reported in **Figure 5**E for MoS_2 thicknesses between 5 and 10 nm closely resemble the results of these experiments.[45] Other groups, too, have shown significant improvements after optimizing the thickness of the MoS_2 catalyst layer.[52] Thus, future work can be devoted to optimizing sample crystallinity, thickness, density, and diameter to equal or better device performance parameters from literature.

The effect of MoS_2 thickness and the source of performance decay with successive cycling were investigated. In **Figure 19**A-B, the linear scan voltammograms of 200 nm MoS_2 nanodisks from immersion coating are shown in order. The decrease in overpotential for 4 nm Mo (126 mV) was less than that for the 1 nm Mo (156 mV), indicating that thickness plays a role in photocathode stability. After 10 successive scans, the samples were removed from the electrochemical cell and treated with 10 wt% HF for 120 s, which replicated the initial surface treatment. After treatment, the performance of the samples returned to their original values, as shown by the dashed black line in **Figure 19**A-B. This indicates that the source of the performance decay is the growth of an insulating oxide layer that increases resistance between

the p-Si and the MoS_2 catalyst layer. The results for 500 nm $MoS2_2$ nanodisks from immersion coating are also shown in **Figure 19**C-D. Compared to 200 nm MoS_2, the influence of thickness on performance decay is more significant with a decrease in overpotential of 31 mV for 4 nm Mo and of 134 mV for 1 nm Mo.

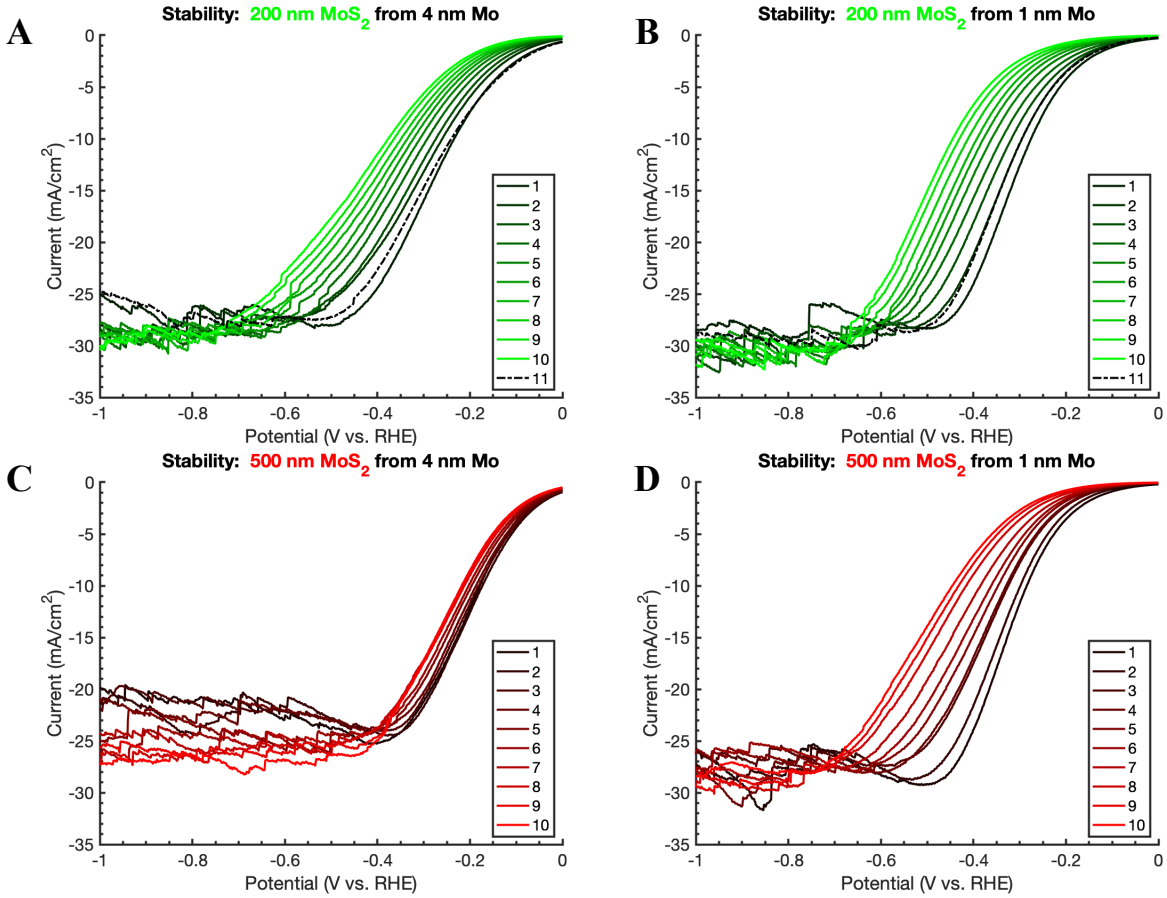

Figure 19: Thickness of MoS_2 nanodisks from immersion coating affects cycling stability. **A:** 200 nm from 4 nm Mo shows potential decrease ΔV= 126 mV compared to ΔV= 156 mV for 1 nm **(B)**. **C:** Effect of thickness for 500 nm is much more significant ΔV= 31 mV for 4 nm compared to ΔV= 134 mV for 1 nm **(D)**.

3.2.3 Two-electrode PEC HER from bare p-Si with optical microscope

Two-electrode tests were conducted to visualize the formation of H_2 bubbles at the p-Si surface using optical microscopy. Without a reference electrode near the surface of the

photocathode, the potential of the electrolyte cannot be measured and varied as it is in three-electrode LSVs. Instead, the source measure unit (SMU) simply applies a variable bias voltage between the anode (Pt foil) and cathode (p-Si) and measures the current. As a result, the bias voltage does not correspond to the potential at the surface of the electrode, and this measurement technique does not account for resistances that vary with bias. Still, the qualitative influence of light intensity was investigated in **Figure 20**C. As the intensity of light from the optical microscope is increased from setting 4 (lowest) to setting 11 (highest), the measured photocurrent increases, as expected. When the intensity of the optical microscope is manually increased from 4 to 10 at a constant bias voltage, the current shows the expected step response (**Figure 20**B). Importantly, the current at constant bias and light intensity appears to drift to more negative values in **Figure 20**B, which is a shortcoming of the two-electrode measurement technique.

Recording video during PEC hydrogen evolution allows the dynamic bubble formation to be observed *in situ*. As shown in **Figure 20**D-E, the nucleation, growth, and disappearance of individual bubbles can be monitored in real-time. Bubbles appear to nucleate repeatedly at the same position, and their size increases to 25 μm at a rate faster than the frame rate of the microscope camera. The individual bubble shown in **Figure 20**D-E increases to a maximum size of 160 μm in 40 s at an optical microscope light setting of 10. After reaching this critical diameter, the bubbles disappeared and began to grow again from the same nucleation site. Previous studies have related the rate of bubble growth to the degree of oversaturation in the electrolyte and have suggested that the spacing between bubbles dictates their relative sizes.[82] If the bubbles are close together they compete with each other for the surrounding H^+ concentration, and larger bubbles begin to form at the expense of their neighbors.[82] As the

bubble in **Figure 20**E reaches a critical size, it depletes the local concentration of H^+ and its volume is added to the larger bubble visible at the top of the frame, which grows throughout testing.

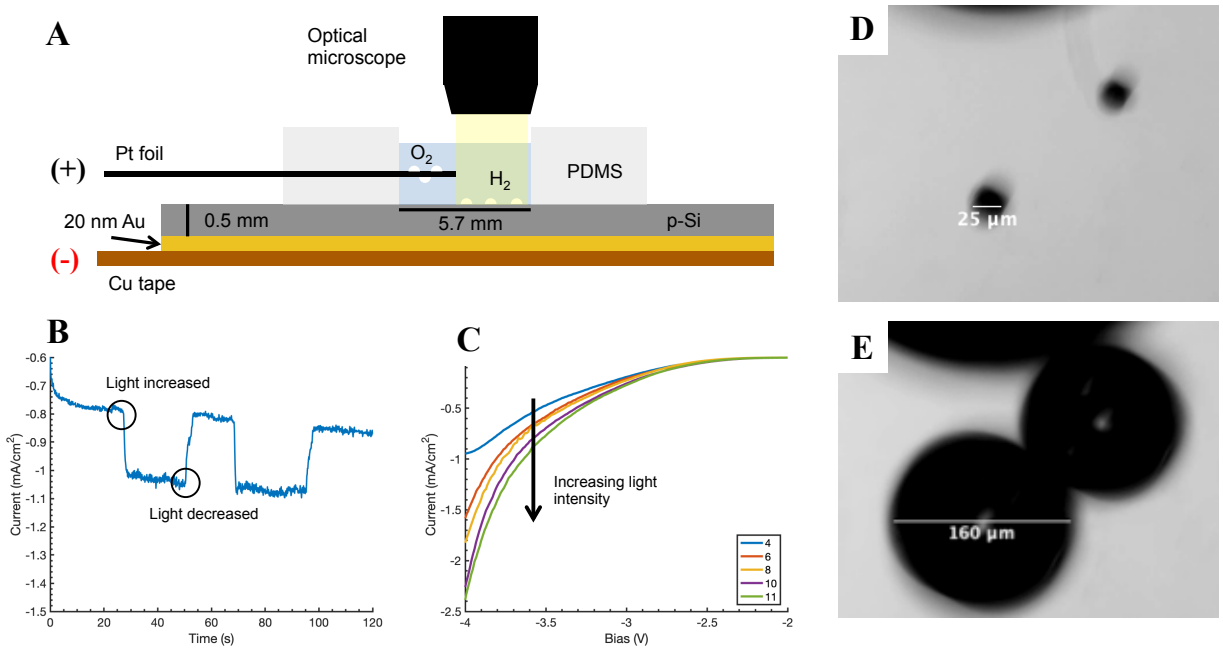

Figure 20: A: Schematic showing experimental setup for PEC hydrogen evolution using light from optical microscope. **B:** CA showing increase in current with manual increases in optical microscope intensity from setting 4 to setting 10. **C:** LSV shows increased current with increased light intensity from 4 (lowest) to 11 (highest). **D:** Images from CA test shown in B. Bubbles repeated nucleated at the same position and increased in size to a maximum diameter of 160 µm.

3.3 Conclusion and Future Work

The photoelectrochemical (PEC) behavior of p-Si was characterized using successive linear scan voltammetry (LSV) and chronoamperometry (CA). The back electrical contact was found to have a significant effect on the performance of bare p-Si. When the metal back contact (Ag two-part epoxy) creates a Schottky barrier due to the mismatch between the metal work function and the Fermi energy of p-Si, the current at -1.0 vs. RHE was measured to be -

20 μA cm^{-2}. Replacing Ag with Ga-In allowed for electron-hole separation and increased the current at -1.0 vs. RHE around 1500x to -35 mA cm^{-2}. Furthermore, replacing Ga-In eutectic with a metal with a sufficiently high work function (Au) decreased the overpotential at -10 mA cm^{-2} from -593 to -390 mV, and Au deposited via e-beam was used on all further samples. The stability of the bare p-Si photocathode was probed by measuring the dark/light current response at a variety of voltages ranging from cathodic (-1.0 V) to short-circuit (0.0 V) to investigate the hypothesis that insulating SiO_2 growth occurred at more anodic voltages. The results agreed with those from successive LSV and indicated that the performance of bare p-Si actually increased with additionally cycling. However, these results should be investigated further with a clearer emphasis on the effect of surface treatment and on the effects of extended cycling (>10 cycles) and long-term stability (CA for >1 hr). Furthermore, increasing the pH of the electrolyte was found to decrease the p-Si photocathode performance in agreement with previous literature.

The PEC performance of continuous MoS_2 films and patterns of MoS_2 nanodisks were compared to that bare p-Si. The preliminary results from continuous MoS_2 films suggest that complete coverage of the Si surface with a conformal catalyst layer substantially reduces photoabsorption and completely hinders the ability of the photocathode to absorb energy from light. These results, however, should be investigated further to address discrepancy with previous reports. Patterns of MoS_2 nanodisks, on the other hand, increased the performance of bare p-Si close to short-circuit voltage. However, he instability of the structures caused a decrease in performance most likely the result of parasitic SiO_2 growth. 500 nm MoS_2 nanodisks showed the lowest overpotential and highest short circuit photocurrent, which does not provide evidence for the hypothesis that HER occurs primarily at the circumferential edges

of the MoS_2. The thickness of the disks was found to influence the cycling stability for both 200 and 500 nm samples. Samples grown from 4 nm Mo showed smaller decreases in overpotential after 10 linear potential scans. Future work will be devoted in optimizing the thickness of MoS_2 to achieve state-of-the-art performance parameters reported in literature. Furthermore, more study, possibly involving before-and-after characterization with Raman spectroscopy and x-ray photoelectron spectroscopy (XPS), is needed to understand the decrease in photocurrent with time. Fabricating a thin (<10 nm) insulating oxide layer, *e.g.* TiO_2 or HfO_2, between the p-Si and MoS_2 catalyst layer with ideal band alignment characteristics may be necessary to create stable photocathodes.

Finally, the *in situ* observation of hydrogen evolution from p-Si via optical microscopy and two-electrode linear potential scans was demonstrated. For applications in colloidal nanomachines, the photocurrent and bubble evolution from p-Si or MoS_2/p-Si can be used to manipulate nanomaterial in solution. If the photocathode is irradiated with a targeted laser with an appropriately small diameter, only the region underneath the laser will generate hydrogen gas and, therefore, will create a localized concentration gradient for the diffusion of H^+ solution. Once the area local to the laser becomes supersaturated with H_2, photocathode-bubble-electrolyte interface can be manipulated as shown in **Figure 20**D-E. Pressure gradients resulting from bubble formation and desorption may be used to direct nanomaterial in solution via a guided laser irradiation pattern.

REFERENCES

1. I. E. Agency, *Key World Energy Statistics 2018*, 2018.

2. E. I. Administration, *International Energy Outlook*, 2017.

3. I. P. o. C. Change, *Climate Change 2014 Synthesis Report Summary for Policymakers*, 2014.

4. I. P. o. C. Change, *Global Warming of 1.5°C: Summary for Policymakers*, 2018.

5. I. E. Agency, *Renewables 2018: Analysis and Forecasts to 2023*, 2018.

6. U. S. D. o. Energy, *The SunShot 2030 Goals*, 2017.

7. S. Chu, Y. Cui and N. Liu, *Nat Mater*, 2016, **16**, 16-22.

8. L. Zhang, Z. J. Zhao and J. Gong, *Angew Chem Int Ed Engl*, 2017, **56**, 11326-11353.

9. M. Gratzel, *Nature*, 2001, **414**, 338-344.

10. R. Parsons, *Transactions of the Faraday Society*, 1958, **54**.

11. J. O. M. Bockris and E. C. Potter, *Journal of The Electrochemical Society*, 1952, **99**.

12. S. Watzele, J. Fichtner, B. Garlyyev, J. N. Schwämmlein and A. S. Bandarenka, *ACS Catalysis*, 2018, **8**, 9456-9462.

13. J. Greeley, T. F. Jaramillo, J. Bonde, I. B. Chorkendorff and J. K. Norskov, *Nat Mater*, 2006, **5**, 909-913.

14. T. F. Jaramillo, K. P. Jorgensen, J. Bonde, J. H. Nielsen, S. Horch and I. Chorkendorff, *Science*, 2007, **317**, 100-102.

15. H. Wang, Z. Lu, S. Xu, D. Kong, J. J. Cha, G. Zheng, P. C. Hsu, K. Yan, D. Bradshaw, F. B. Prinz and Y. Cui, *Proc Natl Acad Sci U S A*, 2013, **110**, 19701-19706.

16. H. Wang, C. Tsai, D. Kong, K. Chan, F. Abild-Pedersen, J. K. Nørskov and Y. Cui, *Nano Research*, 2015, **8**, 566-575.

17. D. Voiry, R. Fullon, J. Yang, E. S. C. de Carvalho Castro, R. Kappera, I. Bozkurt, D. Kaplan, M. J. Lagos, P. E. Batson, G. Gupta, A. D. Mohite, L. Dong, D. Er, V. B. Shenoy, T. Asefa and M. Chhowalla, *Nat Mater*, 2016, **15**, 1003-1009.

18. J. Ma, X. Li, L. Gan, S. Zhang, Y. Cao, Z. Nie, X. Wang, D. Ma, L. He, J. Nie, C. Xiong and R. Dou, *2D Materials*, 2018, **5**.

19. D. Kong, H. Wang, J. J. Cha, M. Pasta, K. J. Koski, J. Yao and Y. Cui, *Nano Lett*, 2013, **13**, 1341-1347.

20. J. Bonde, P. G. Moses, T. F. Jaramillo, J. K. Nørskov and I. Chorkendorff, *Faraday Discuss.*, 2009, **140**, 219-231.

21. G. Ye, Y. Gong, J. Lin, B. Li, Y. He, S. T. Pantelides, W. Zhou, R. Vajtai and P. M. Ajayan, *Nano Lett*, 2016, **16**, 1097-1103.

22. H. Li, C. Tsai, A. L. Koh, L. Cai, A. W. Contryman, A. H. Fragapane, J. Zhao, H. S. Han, H. C. Manoharan, F. Abild-Pedersen, J. K. Norskov and X. Zheng, *Nat Mater*, 2016, **15**, 48-53.

23. Y. Ouyang, C. Ling, Q. Chen, Z. Wang, L. Shi and J. Wang, *Chemistry of Materials*, 2016, **28**, 4390-4396.

24. R. J. Toh, Z. Sofer, J. Luxa, D. Sedmidubsky and M. Pumera, *Chem Commun (Camb)*, 2017, **53**, 3054-3057.

25. J. Shi, D. Ma, G. F. Han, Y. Zhang, Q. Ji, T. Gao, J. Sun, X. Song, C. Li, Y. Zhang, X. Y. Lang, Y. Zhang and Z. Liu, *ACS Nano*, 2014, **8**, 10196-10204.

26. X. Li and H. Zhu, *Journal of Materiomics*, 2015, **1**, 33-44.

27. A. J. Bard, M. Stratmann, D. Macdonald and P. Schmuki, *Encyclopedia of Electrochemistry: Electrochemical Engineering; Volume 5*, Wiley-VCH, 2007.

28. Y. Wan, Z. Zhang, X. Xu, Z. Zhang, P. Li, X. Fang, K. Zhang, K. Yuan, K. Liu, G. Ran, Y. Li, Y. Ye and L. Dai, *Nano Energy*, 2018, **51**, 786-792.

29. Q. Huang, Z. Ye and X. Xiao, *Journal of Materials Chemistry A*, 2015, **3**, 15824-15837.

30. E. L. Warren, H. A. Atwater and N. S. Lewis, *The Journal of Physical Chemistry C*, 2013, **118**, 747-759.

31. J. T. Davis, J. Qi, X. Fan, J. C. Bui and D. V. Esposito, *International Journal of Hydrogen Energy*, 2018, **43**, 1224-1238.

32. A. J. Nozik and R. Memming, *The Journal of Physical Chemistry*, 1996, **100**, 13061-13078.

33. M. X. Tan, P. E. Laibinis, S. T. Nguyen, J. M. Kesselman, C. E. Stanton and N. S. Lewis, in *Progress in Inorganic Chemistry*, 2007, DOI: 10.1002/9780470166420.ch2, pp. 21-144.

34. S. Giménez and J. Bisquert, *Photoelectrochemical solar fuel production*, Springer, 2016.

35. A. J. Bard, A. B. Bocarsly, F. R. F. Fan, E. G. Walton and M. S. Wrighton, *Journal of the American Chemical Society*, 1980, **102**, 3671-3677.

36. H. Kisch, *Semiconductor photocatalysis : principles and applications*, Wiley-VCH, Weinheim, Germany, 2015.

37. R. Memming, *Semiconductor electrochemistry*, John Wiley & Sons, 2015.

38. H. Zimmermann, *Integrated silicon optoelectronics*, Springer, 2010.

39. S. W. Boettcher, E. L. Warren, M. C. Putnam, E. A. Santori, D. Turner-Evans, M. D. Kelzenberg, M. G. Walter, J. R. McKone, B. S. Brunschwig, H. A. Atwater and N. S. Lewis, *J Am Chem Soc*, 2011, **133**, 1216-1219.

40. Q. Ding, B. Song, P. Xu and S. Jin, *Chem*, 2016, **1**, 699-726.

41. K. Sun, S. Shen, Y. Liang, P. E. Burrows, S. S. Mao and D. Wang, *Chem Rev*, 2014, **114**, 8662-8719.

42. P. Würfel and U. Würfel, *Physics of solar cells: from basic principles to advanced concepts*, John Wiley & Sons, 2016.

43. N. S. Lewis, *Annual review of physical chemistry*, 1991, **42**, 543-580.

44. B. Seger, A. B. Laursen, P. C. Vesborg, T. Pedersen, O. Hansen, S. Dahl and I. Chorkendorff, *Angew Chem Int Ed Engl*, 2012, **51**, 9128-9131.

45. K. C. Kwon, S. Choi, K. Hong, C. W. Moon, Y.-S. Shim, D. H. Kim, T. Kim, W. Sohn, J.-M. Jeon, C.-H. Lee, K. T. Nam, S. Han, S. Y. Kim and H. W. Jang, *Energy & Environmental Science*, 2016, **9**, 2240-2248.

46. R. Fan, J. Mao, Z. Yin, J. Jie, W. Dong, L. Fang, F. Zheng and M. Shen, *ACS Appl Mater Interfaces*, 2017, **9**, 6123-6129.

47. Y. Hou, B. L. Abrams, P. C. Vesborg, M. E. Bjorketun, K. Herbst, L. Bech, A. M. Setti, C. D. Damsgaard, T. Pedersen, O. Hansen, J. Rossmeisl, S. Dahl, J. K. Norskov and I. Chorkendorff, *Nat Mater*, 2011, **10**, 434-438.

48. M. J. Choi, J.-Y. Jung, M.-J. Park, J.-W. Song, J.-H. Lee and J. H. Bang, *Journal of Materials Chemistry A*, 2014, **2**.

49. K. C. Kwon, S. Choi, K. Hong, D. M. Andoshe, J. M. Suh, C. Kim, K. S. Choi, J. H. Oh, S. Y. Kim and H. W. Jang, *MRS Communications*, 2017, **7**, 272-279.

50. D. M. Andoshe, G. Jin, C.-S. Lee, C. Kim, K. C. Kwon, S. Choi, W. Sohn, C. W. Moon, S. H. Lee, J. M. Suh, S. Kang, J. Park, H. Heo, J. K. Kim, S. Han, M.-H. Jo and H. W. Jang, *Advanced Sustainable Systems*, 2018, **2**.

51. J. Zhou, S. Dai, W. Dong, X. Su, L. Fang, F. Zheng, X. Wang and M. Shen, *Applied Physics Letters*, 2016, **108**.

52. J. Joe, C. Bae, E. Kim, T. A. Ho, H. Yang, J. H. Park and H. Shin, *Catalysts*, 2018, **8**.

53. K. Ariga, J. P. Hill and Q. Ji, *Phys Chem Chem Phys*, 2007, **9**, 2319-2340.

54. N. Denkov, O. Velev, P. Kralchevski, I. Ivanov, H. Yoshimura and K. Nagayama, *Langmuir*, 1992, **8**, 3183-3190.

55. J. Chen, P. Dong, D. Di, C. Wang, H. Wang, J. Wang and X. Wu, *Applied Surface Science*, 2013, **270**, 6-15.

56. J. Guo, K. Kim, K. W. Lei and D. L. Fan, *Nanoscale*, 2015, **7**, 11363-11370.

57. M. Bosi, *RSC Advances*, 2015, **5**, 75500-75518.

58. L. Ji, M. D. McDaniel, S. Wang, A. B. Posadas, X. Li, H. Huang, J. C. Lee, A. A. Demkov, A. J. Bard, J. G. Ekerdt and E. T. Yu, *Nat Nanotechnol*, 2015, **10**, 84-90.

59. J. M. K. Ng, I. Gitlin, A. D. Stroock and G. M. Whitesides, *Electrophoresis*, 2002, **23**, 3461-3473.

60. J. H. Parker, D. W. Feldman and M. Ashkin, *Physical Review*, 1967, **155**, 712-714.

61. C. Lee, H. Yan, L. E. Brus, T. F. Heinz, J. Hone and S. Ryu, *ACS Nano*, 2010, **4**, 2695-2700.

62. Y. Zhan, Z. Liu, S. Najmaei, P. M. Ajayan and J. Lou, *Small*, 2012, **8**, 966-971.

63. A. E. Dorfi, A. C. West and D. V. Esposito, *The Journal of Physical Chemistry C*, 2017, **121**, 26587-26597.

64. Z. Chen, H. N. Dinh and E. Miller, *Photoelectrochemical Water Splitting*, 2013.

65. J. Riviere, *Solid State Surface Science*, 1969, **1**.

66. D. A. Neamen, *Semiconductor physics and devices: basic principles*, New York, NY: McGraw-Hill, 2012.

67. J. Oh, T. G. Deutsch, H.-C. Yuan and H. M. Branz, *Energy & Environmental Science*, 2011, **4**.

68. I. Oh, J. Kye and S. Hwang, *Nano Lett*, 2012, **12**, 298-302.

69. B. Sopori, V. Mehta, P. Rupnowski, H. Moutinho, A. Shaikh, C. Khadilkar, M. Bennett and D. Carlson, *MRS Proceedings*, 2011, **1123**.

70. U. Sim, J. Moon, J. Lee, J. An, H. Y. Ahn, D. J. Kim, I. Jo, C. Jeon, S. Han, B. H. Hong and K. T. Nam, *ACS Appl Mater Interfaces*, 2017, **9**, 3570-3580.

71. U. Sim, J. Moon, J. An, J. H. Kang, S. E. Jerng, J. Moon, S.-P. Cho, B. H. Hong and K. T. Nam, *Energy & Environmental Science*, 2015, **8**, 1329-1338.

72. R. N. Dominey, N. S. Lewis, J. A. Bruce, D. C. Bookbinder and M. S. Wrighton, *Journal of the American Chemical Society*, 1982, **104**, 467-482.

73. S. R. German, M. A. Edwards, Q. Chen and H. S. White, *Nano Lett*, 2016, **16**, 6691-6694.

74. S. R. German, M. A. Edwards, H. Ren and H. S. White, *J Am Chem Soc*, 2018, **140**, 4047-4053.

75. P. Pichler, *Intrinsic Point Defects, Impurities, and Their Diffusion in Silicon*, 2004.

76. A. Mostafa and M. Medraj, *Materials (Basel)*, 2017, **10**.

77. A. P. Goodey, S. M. Eichfeld, K. K. Lew, J. M. Redwing and T. E. Mallouk, *J Am Chem Soc*, 2007, **129**, 12344-12345.

78. C. G. Morales-Guio, S. D. Tilley, H. Vrubel, M. Gratzel and X. Hu, *Nat Commun*, 2014, **5**, 3059.

79. I. Roger, M. A. Shipman and M. D. Symes, *Nature Reviews Chemistry*, 2017, **1**.

80. J. D. Benck, S. C. Lee, K. D. Fong, J. Kibsgaard, R. Sinclair and T. F. Jaramillo, *Advanced Energy Materials*, 2014, **4**.

81. Q. Ding, F. Meng, C. R. English, M. Caban-Acevedo, M. J. Shearer, D. Liang, A. S. Daniel, R. J. Hamers and S. Jin, *J Am Chem Soc*, 2014, **136**, 8504-8507.

82. S. Peng, T. L. Mega and X. Zhang, *Langmuir*, 2016, **32**, 11265-11272.